Universidade de São Paulo
Instituto de Astronomia, Geofísica e Ciências Atmosféricas
Departamento de Astronomia

Matheus Zaghi de Oliveira

Magnetospheres around High Mass Stars revealed by Polarimetry

São Paulo
2022

Matheus Zaghi de Oliveira

Magnetospheres around High Mass Stars revealed by Polarimetry

Dissertação apresentada ao Departamento de Astronomia do Instituto de Astronomia, Geofísica e Ciências Atmosféricas da Universidade de São Paulo como requisito parcial para a obtenção do título de Mestre em Ciências.

Área de Concentração: Astronomia
Orientador(a): Prof. Dr. Alex C. Carciofi

Versão corrigida. O original encontra-se disponível na Unidade.

São Paulo

2022

a minha mãe

Acknowledgements

Primeiramente, quero agradecer aos meus pais, Ordemir e Regina. Apesar da distância e de nos reunirmos poucas vezes ao ano, o apoio, suporte e amor que me dão foram e são fundamentais em todos os aspectos de minha vida.

Gostaria de agradecer também aos meus irmãos, Cassiano e Lucca. Todas as divertidas conversas e distrações ajudaram a manter a alegria durante o longo e difícil período de pandemia.

Ao professor Alex Carciofi, que, além de ser um ótimo orientador, se tornou um grande companheiro. Seus conselhos foram de grande impacto em minha formação e vão além do limite acadêmico.

À todos os membros da minha família, Andreia, Júnior, Jaime, Lilian, Luiza e Silvia. Em especial ao Humberto, sempre preocupado com minha condição financeira e me ajudando da melhor maneira possível. À minha avó Silvia, por sempre organizar agradáveis encontros familiares. Também aos meus primos Vinícius, Jaime e Marlene, e às novas membros da família, Alice e Maria Luiza.

Ao meu grande amigo Rafael Fernandes, pelas conversas, risadas e conselhos durante longas caminhadas.

À Stela, pelo suporte e companheirismo durante todos esses anos de USP. Sua parceria e palavras de motivação foram fundamentais para a conclusão deste projeto.

À todos os membros do grupo BeACoN, em especial à Ariane Cristina. Todo seu cuidado e paciência durante as reduções dos dados foram de fundamental importância para este projeto, além de ser uma ótima companheira de viagem.

À relatora Vera Jatenco, pelo seus comentários e sugestões sobre o trabalho, além de contribuir para minha formação com o curso de Formação Estelar.

À todos os funcionários do OPD, pelo suporte e atenção durante as missões.

Ao Diogo Frogeri, por ser o melhor colega de apartamento que alguém poderia pedir.

À todos os funcionários do IAG, pessoal da informática, da secretaria da Astronomia, da secretaria de pós-graduação. Aos funcionários terceirizados da portaria e da faxina, por manter o IAG um lugar seguro e organizado.

À Capes pelo suporte financeiro e pela extensão do período de bolsa.

À CCP da Astronomia pelo auxílio PROEX para a participação de congresso no exterior.

Por fim, ao meu grande amigo Chibi. Apesar de não estar mais entre nós, sua alegria e empolgação será sempre lembrada com carinho.

Esta dissertação foi escrita em LaTeX com a classe IAGTESE, para teses e dissertações do IAG.

"*The two most important days in your life are the day are born and the day you find out why.*"

Mark Twain

Resumo

Aproximadamente 10% das estrelas massivas conhecidas possuem campo magnético de força relevante. Combinado a uma rápida rotação da estrela, campos magnéticos podem ser capazes de aprisionar o material expelido, o forçando a corrotacionar com a estrela, criando as chamadas magnetosferas. O modelo *Rigidly Rotating Magnetosphere* (RRM) foi criado para o caso de campos fortes e altas velocidades de rotação. Ele, porém, não é capaz de reproduzir simultaneamente fotometria e polarimetria da estrela arquétipo σ Ori E. Um modelo alternativo, chamado *Dumbbell plus Disk* (D+D) foi proposto, que permite um bom ajuste dos dados polarimétricos e a definição de parâmetros básicos da magnetosfera. Apresentamos o resultado de um monitoramento polarimétrico de estrelas massivas magnéticas no Observatório Pico dos Dias, onde foram realizadas observações de 18 estrelas nos filtros V e R. Aprimoramos o método de ajuste do modelo D+D, acoplando a rotina original ao algoritmo *emcee* do método de Monte Carlo via Cadeias de Markov, possibilitando uma análise estatística mais robusta dos dados. O objetivo do projeto é obter dados da polarização linear de estrelas massivas magnéticas durante todo seu período de rotação, e assim aplicar o modelo D+D para estudar suas magnetosferas. Reportamos a detecção de quatro novas magnetosferas por polarimetria, nas estrelas HD 35502, HD 142990, HR 7355 e HR 5907. Aplicamos o modelo aos dados observacionais, onde aprimoramos os resultados de σ Ori E. Das novas detecções, duas estrelas, HD 35502 e HD 142990 tiveram bons ajustes, permitindo determinar os parâmetros de suas magnetosferas. HR 7355 e HR 5907 tiveram ajustes marginais, que podem ser causados pela baixa modulação da polarização intrínseca, ou pela inadequação do D+D para estes objetos. Também foi feita uma análise para investigar relações existentes entre as propriedades da magnetosfera e sua estrela. Encontramos que a massa da magnetosfera aumenta com a força do campo magnético.

Abstract

About 10% of the known massive stars have a magnetic field of relevant strength. Combined with the star's fast rotation, the magnetic field may be able to trap the expelled material, forcing it to corotate with the star, creating the so-called magnetospheres. The *Rigidly Rotating Magnetosphere* (RRM) model was created for the case of strong magnetic fields and high rotation velocity. However, it is not able to simultaneously reproduce the photometry and polarimetry of the archetype star σ Ori E's magnetosphere. An alternative model, named *Dumbbell plus Disk* (D+D) was proposed, which allows a good fit of the data and the determination of basic parameters of the magnetosphere. We present the results of a polarimetric survey of massive magnetic stars at Pico dos Dias Observatory (OPD), where observations of 18 stars were carried out int the V and R filters. We improved the fitting method of the D+D model, coupling the original routine to the *emcee* algorithm of the Monte Carlo Markov Chain method, making possible a more robust statistical analysis of the data. The objective of the project is to obtain linear polarization data of massive magnetic stars throughout their rotation period, and thus apply the D+D model to study their magnetospheres. We report the detection of four new magnetospheres by polarimetry, in the stars σ Ori E, HD 35502, HD 142990, HR 7355, and HR 5907. We applied the model to observational data and improved the results of σ Ori E. Of the new detections, two stars, HD 35502 and HD 142990 had good fits, making it possible to determine the parameters of their magnetospheres. HR 7355 and HR 5907 had marginal fits, which can be caused by the low modulation of the intrinsic polarization, or by the inadequacy of the D+D for these objects. An analysis was also made to investigate existing relations between the properties of the magnetosphere and its host star. We found that the mass of the magnetosphere increases with the strength of the magnetic field.

List of Figures

List of Tables

Contents

Chapter 1

Introduction

1.1 Massive Stars

The measurement of stellar masses began with the discovery of eclipsing binary stars and the determination of stellar spectral types. It was realized by the middle of the XIX century that stars come in a wide range of masses, ranging from about $0.1M_{\odot}$ to more than $80M_{\odot}$. Stars with an initial mass greater than $8M_{\odot}$ are called massive stars. They constitute only about 10% of all stellar mass fraction, and only about 0.2% in number (Meyers, 2002).

Unlike low mass stars, the pressure and temperature of high mass stars can reach high enough values that the fusion of carbon and heavier elements up to iron at their core happens. Massive stars end their lives in gigantic explosions called supernovae and are responsible for the creation of the heaviest elements in the Universe. However, the core of stars with 17 to $30M_{\odot}$ may form black-holes without an explosion or a weak one that will remain undetected (Smartt, 2009).

On the main sequence, a massive star's high effective temperature and luminosity result in strong stellar winds, which are driven by radiation pressure, producing significant mass loss (Castor et al., 1975). As a result, they lose mass at rates that grow with their initial mass.

Massive stars affect the overall evolution and properties of the galaxies through feedback mechanisms (Livio and Villaver, 2009). Their ultraviolet radiation heats dust, powering the far-IR luminosities of galaxies (Maeder and Conti, 1994) and their strong stellar winds provide significant mechanical energy input into the interstellar medium, as does their eventual disruption as supernovae, shock-heating the gas to $> 10^6$ K (Livio and Villaver,

2009). Also, massive stars are responsible for much of the chemical enrichment of galaxies, particularly of the lighter elements, such as carbon, nitrogen, and oxygen (Maeder, 1981).

1.2 Magnetic Massive Stars

New generations of spectropolarimeters have directly revealed that, in addition to low-mass stars, for which they are known, magnetic fields also occur in massive stars. In recent years, several surveys have been carrying observations of OB stars in search of the presence of magnetic fields. The most direct and reliable method to detect the magnetic field of hot stars is through Zeeman splitting and associated circular polarization of stellar photospheric absorption lines (Borra and Landstreet, 1980).

Carried out in recent years, the observational consortium known as MiMeS (Magnetism in Massive Stars, Wade et al., 2013) was by far the largest systematic survey of massive star magnetism ever undertaken. The project was a large-scale, high-resolution, sensitive spectropolarimetric investigation of the magnetic properties of O and early B-type stars that started in 2008 and ended in 2013. The survey collected over 4800 circularly polarized spectra of 560 O and B stars.

The results of the survey show that about 10% of the stars observed have a reliable magnetic field detection (Wade et al., 2016). Also, in contrast to the magnetic fields of cool stars, which tend to display complex surface topology, the strength of a few kGs, as well as magnetic activity cycles associated with dynamos, the magnetic fields of early-type stars have the following characteristics:

- they tend to be strong (typically raging from a 0.1 to 15 kG, but can reach values of about 30kG at the stellar surface).
- they are stable, not showing any considerable change over the time-spans of years to decades.
- they have an important dipolar component that dominates the field, but some stars can have a more complex topology.

Monitoring of the longitudinal field[1] variations provides a natural and direct way to determine rotational periods for magnetic stars (in the context of the Oblique Rotator

[1] Longitudinal field is the component of the magnetic field that is parallel to its dipole axis

Model, Stibbs, 1950). Photometric and spectral variability associated with the magnetic field also provides a convenient and easy way to determine periods.

Since observed fields have large-scale, quasi-static, stable configurations, which are not correlated with the star's characteristics such as rotation, it is believed that the field has a fossil origin. The hypothesis of fossil fields requires that they were already present before the star reached the main sequence. It is necessary for a stable poloidal-toroidal field configuration, as analytical results showed not so long ago (Braithwaite and Spruit, 2004), for it to exist long enough without being replenished by a dynamo. Numerical simulations provided the first evidence of such a stable field configuration (Zahn et al., 2007). For more details on fossil fields of massive stars, see Walder et al. (2012) and references therein.

The high luminosity of massive stars can cause powerful winds. Magnetohydrodynamic simulations show that a dipolar magnetic field of large scale can trap such winds in closed loops along the magnetic field lines (Ud-Doula et al., 2002). The influence of the field upon the wind can be characterized by a single parameter, named *magnetic-confinement parameter*:

$$\eta_* = \frac{B_{\rm eq}^2 R_*^2}{\dot{M}_{B=0} V_\infty}, \tag{1.1}$$

where $B_{\rm eq}$ is the strength of the field at the rotational equator R_*, $\dot{M}_{\rm B=0}$ and V_∞ are the fiducial mass loss and terminal velocity that the star would have without the magnetic field.

For weak confinements, where $\eta_* \leq 1$, the field is fully opened by the wind outflow. However, for strong confinements, $\eta_* > 10$, the field remains with closed loops near the equatorial surface, and the outflow is trapped by closed loops within the Alfvén radius, forming a wind-fed *magnetosphere*. Wind outflows accelerated radially from opposite polarity footpoints are channeled near the loop tops into collisions strong enough that are capable to produce X-rays.

This confinement parameter determines the scale between magnetic energy density and kinetic energy of the wind. For a dipole field, the r^{-6} radial decline of magnetic energy is much steeper than the r^{-2} decline of the wind's mass and energy density. This means the wind always dominates beyond the Alfvén radius (the point where the magnetic energy density is equal to the kinetic energy density), given by the approximation (Ud-Doula et al., 2008)

$$\frac{R_{\rm A}}{R_*} \approx 0.3 + (\eta_* + 0.25)^{1/4}. \tag{1.2}$$

Magnetic loops that extend beyond the $R_{\rm A}$ are open by the wind, while those inside $R_{\rm A}$ will remain closed.

Rotation adds a layer of complication to the problem, as the wind material is forced by the magnetic field to corotate with the star (Ud-Doula et al., 2008). The parameter that is usually used to describe stellar rotation is the dimensionless rotation parameter:

$$W = \frac{V_{\rm rot}}{V_{\rm orb}}, \tag{1.3}$$

where $V_{\rm orb} = \sqrt{GM/R_*}$ is the orbital speed near the equatorial surface and $V_{\rm rot}$ is the rotation speed at the equatorial surface. If $W = 1$, the azimuthal speed at the equator is such that the outward centrifugal force balances the surface gravity. In a magnetic star with a sufficiently strong magnetic field, magnetic torques on the wind can spin up the material, so that it can even maintain a rigid-body rotation up to the Alfvén radius. Therefore, the azimuthal speed of the confined wind plasma increases with radius.

The centrifugal force from such rigid-body rotation will balance the inward force of gravity at the *Keplerian corotation radius*

$$R_{\rm K} \equiv \left(\frac{GM}{\omega^2}\right)^{1/3} = W^{-2/3} R_*. \tag{1.4}$$

where ω is the angular velocity. The parameters η_* and W will then define the relative locations of the Alfvén and Kepler radii with respect to the equatorial radius.

The classification for magnetospheres was proposed by Petit et al. (2013), and is based on the relative values for $R_{\rm K}$ and $R_{\rm A}$. A schematic representation is shown in Fig. 1.1.

If $R_{\rm K} > R_{\rm A}$, the star has a *dynamical magnetosphere* (DM), characterized by weak rotation and/or magnetic confinement, with the effects of rotation limited to some modest enhancement in equatorial density. In general, any magnetically confined material falls back to the star in a dynamical timescale.

If $R_{\rm K} < R_{\rm A}$, the strong magnetic confinement combines with a sufficiently rapid rotation that can support the material against infall near the Keplerian corotation radius. The magnetic field and centrifugal force both hold the material in nearly rigid-body rotation

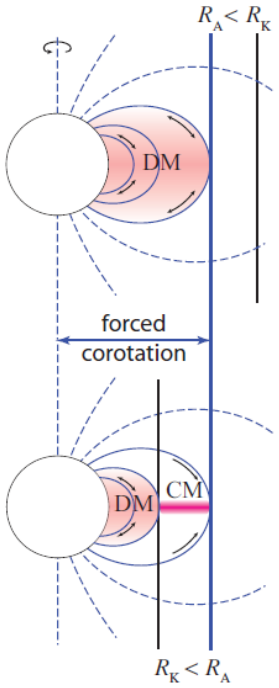

Figure 1.1: Schematic representation of dynamical (top) and centrifugal (bottom) magnetospheres. If the star rotates fast enough, the wind material is trapped by the magnetic field and forced to corotate with the star, thus forming a magnetosphere. Image adapted from Petit et al. (2013).

and keep it confined against the tendency of the material to escape the system, building a much denser magnetosphere. In this case, we have a *centrifugal magnetosphere* (CM).

Transition models with $R_K \approx R_A$ have a complex combination of inner region infall and outer region breakout but show no signs of accumulation of material inwards the Keplerian corotation radius.

Figure 1.2 shows a sample of massive magnetic stars in the magnetic confinement-rotation diagram. It is a log-log plane with R_K/R_* increasing downwards vs. R_A/R_*. The vertical line $\eta_* = 1$ ($R_A/R_* \approx 1.3$) separates weakly magnetized winds from the domain of stars with significant magnetospheres. The diagonal line separates stars with CM from stars with DM. In this work, we are focusing on stars with strong magnetic fields and short rotation periods, i.e., stars with centrifugal magnetospheres, that are located in the upper-right corner of the diagram.

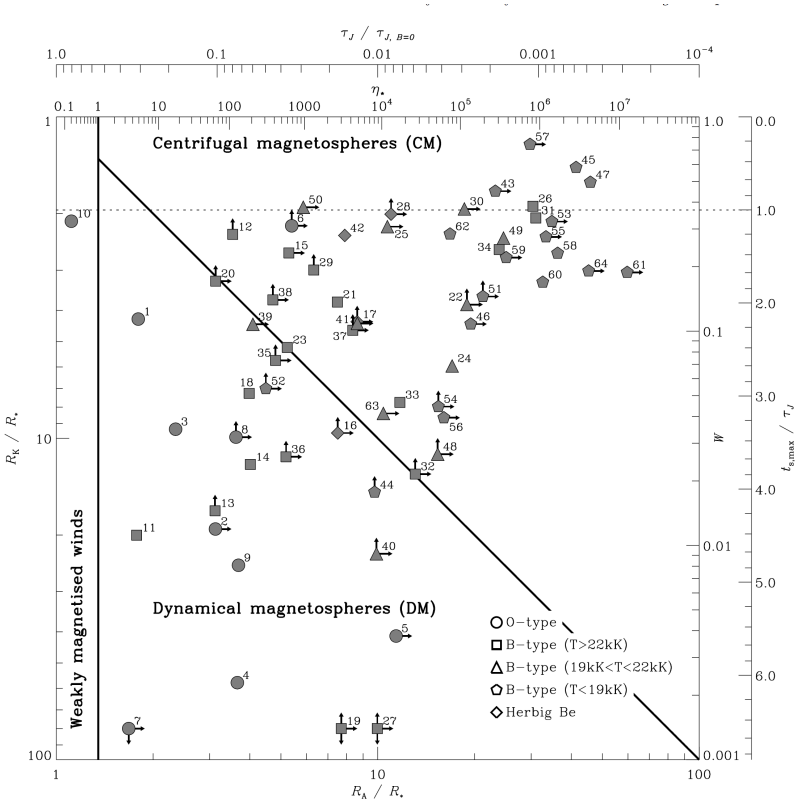

Figure 1.2: Confinement-diagram rotation showing the location of massive magnetic stars. Note that a massive star with a strong magnetic field cannot support a CM if its rotational velocity is not fast enough. Image adapted from Petit et al. (2013).

1.2.1 Modeling Magnetospheres

A model named Rigidly-Rotating Magnetosphere (RRM) showed some success in modeling the circumstellar material of stars with centrifugal magnetospheres. The model was applied to σ Ori E (Townsend et al., 2005) and was able to reproduce the observational peculiarities created by the expected clouds that eclipse the star twice during its 1.19 day period (Fig. 1.3). We will talk in more detail about the RRM model in Section 2.1.

However, a following work (Carciofi et al., 2013) performed the first detection of a magnetosphere through linear polarization. The work also showed that the RRM fails at reproducing the linear polarization of σ Ori E. The authors created a new *ad hoc* model, named Dumbbell plus Disk, and were able to reproduce the observed linear polarization of the star, as well as deduce the mass of the components of the magnetosphere (more details of the model in Section 2.3). So far, σ Ori E is the first and only detection of a massive star magnetosphere through polarization.

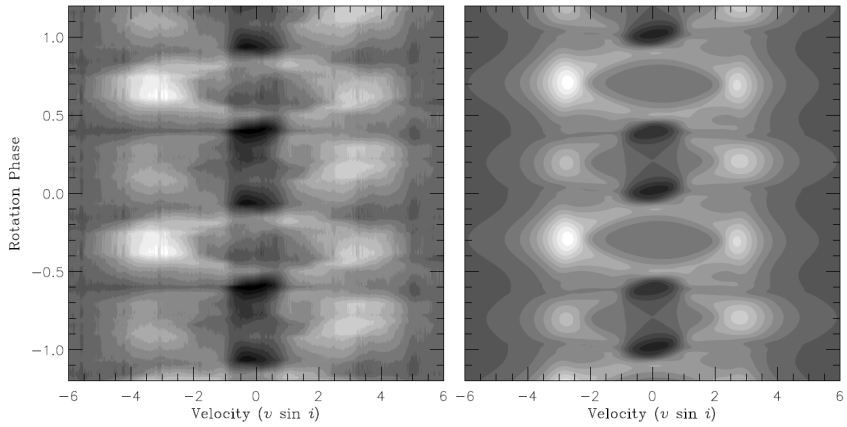

Figure 1.3: Phased periodic line profile variability of the observed (left) and modeled (right) H α emission of σ Ori E, phased on the star rotation period of 1.19 days. White region is a 22% excess, in continuum units, over the background photospheric flux, and black indicates a 12% deficit. Gray regions are linear scales of the values between the extremes. The velocity axis is expressed in units of $v \sin i = 160\,\mathrm{km\,s^{-1}}$ (Groote and Hunger, 1982). Image from Townsend et al. (2005).

1.2.2 Objectives

The objective of this work is to study the CMs of OB stars through their linear polarization. More precisely, we intend to expand the list of centrifugal magnetospheres detected with linear polarization and to use the observational data to model the magnetospheres using the Dumbbell plus Disk model. Since polarimetry is very sensitive to the density of the magnetosphere (and also its geometry), determining this parameter for a larger sample of stars will help us to unveil how the intrinsic stellar parameters, such as rotation rate, mass, and magnetic field strength, affects the magnetosphere itself. This will provide important information on future attempts to expand the RRM model and make it more realistic.

Our polarimetric observations can, in the future, be coupled with other data already available for these systems, such as photometry and spectroscopy, in order to make even more stringent constraints to models.

Broadly speaking, the results of this MSc work will help shed light on the complex physics of the interaction between plasma flows (i.e., stellar wind in this case) and strong magnetic fields.

Chapter 2

Theoretical Considerations

In this chapter, we address some of the most important theoretical aspects of this work. In Sec. 2.1, we give more details about the Rigidly-Rotating Magnetosphere model, upon which this work is based. In Sec. 2.2, we discuss in detail linear polarization and how it can be generated in circumstellar material. Sec. 2.3 describes the modeling process and Sec. 2.4 the new statistical treatment applied to the model.

2.1 Rigidly Rotating Magnetosphere Model

Several models have been proposed to study the properties of centrifugal magnetospheres of massive stars. MHD simulations of the magnetically confined wind shock (MCWS) have been applied to the O7pe star θ^1 Ori C and were able to reproduce its observed X-ray properties successfully (Donati et al., 2002).

The model that more reliably reproduces the centrifugal magnetosphere of high-mass, highly magnetic stars is the Rigidly-Rotating Magnetosphere (RRM, Townsend and Owocki, 2005). The RRM model was created on the notion that the plasma flowing along the magnetic field lines experiences an effective potential arising from a combination of the stellar gravitational field and the centrifugal forces due to corotation.

The plasma, flowing along the field lines, settles in the vicinity of the points where the potential undergoes a local minimum. In the case of a centered dipole magnetic field aligned with the star's rotation axis, the potential is given by:

$$\Psi(r) \equiv \frac{GM_*}{R_{\rm K}} \left(-\frac{1}{\xi} - \frac{1}{2}\xi^2 \sin^2\theta \right), \tag{2.1}$$

where $\xi \equiv r/R_K$ is the radial coordinate in units of Keplerian corotation radius. However,

in most cases, the dipole magnetic field is tilted by an angle β with respect to the rotation axis. For such geometry, the potential is then given by:

$$\Psi(\tilde{\theta}) = -\frac{1}{\gamma \sin^2 \tilde{\theta}} - \frac{1}{2}\gamma^2 \sin^4 \tilde{\theta} \left[\sin^2 \tilde{\theta} \sin^2 \tilde{\phi} + \left(\sin\beta \cos\tilde{\theta} + \cos\beta \sin\tilde{\theta} \cos\tilde{\phi}\right)^2\right], \quad (2.2)$$

where the parameter γ specifies the summit radius in units of R_K of the field line, $\tilde{\theta}$ is the colatitude coordinate in the frame of reference aligned with the magnetic axis and ϕ denotes the azimuthal coordinate in the magnetic frame.

Figure 2.1 shows the effective potential plots for dipole field configurations tilted at angles $\beta = 30°$, $\beta = 60°$ and $\beta = 90°$. For each geometry of the magnetic field, the effective potential has a different configuration. For $\beta = 30°$ and $\beta = 60°$, the minima are situated at approximately the same colatitude, around $\tilde{\theta} = 75°$. In the case of $\beta = 90°$, we see two minima occurring in the potential along the outer field lines, at $\tilde{\theta} = 55°$ and $\tilde{\theta} = 125°$. Figs. 2.2 and 2.3 illustrate the accumulation surfaces for each case of β. For $\beta = 0$, the surface is a disk situated at the rotational and magnetic equators. As β increases, the surface becomes more warped, while still resembling a disk. For $\beta = 60°$, a pair of accumulations, called *leaves*, appear in both hemispheres between the magnetic and rotation axis. To a perpendicular field $\beta = 90°$, the surface takes the shape of a combination of a disk at the magnetic equator and two cones aligned with the rotation axis.

The RRM model shows that the magnetospheres of fast-rotating magnetic massive stars with dipole magnetic field can be quite complex and that for different values for the obliquity β, we expect different configurations.

The RRM model was first applied to the archetype star σ Ori E (Townsend et al., 2005). The model was able to reproduce the magnetic, spectroscopic, and photometric variability of the star during its 1.19 day period. The model is capable of giving a qualitative description of the star's magnetically confined circumstellar material. However, as seen below in Sec. 2.3, the RRM model failed to reproduce the modulation of both the polarization level and angle.

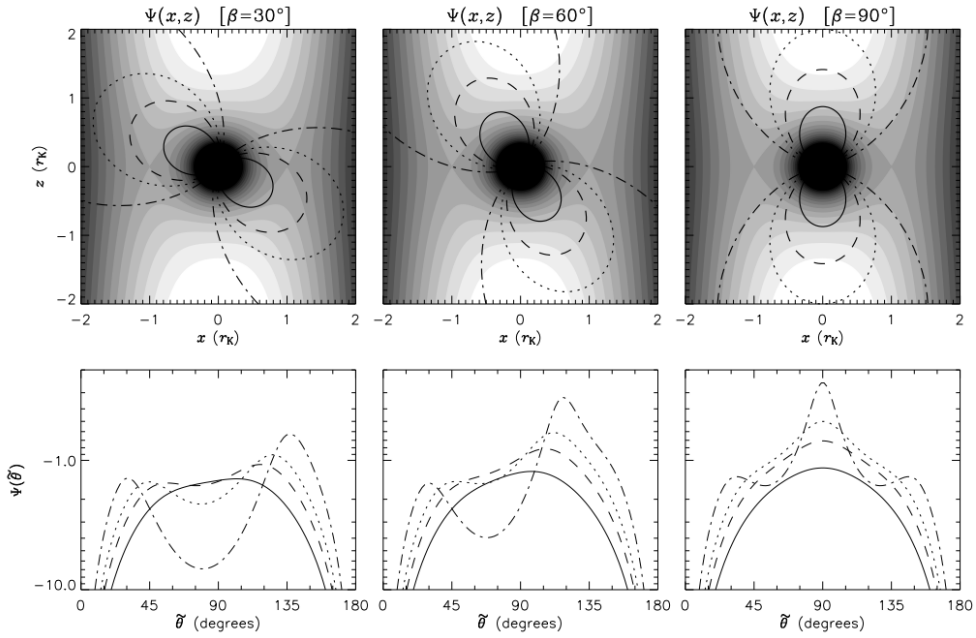

Figure 2.1: Contour map of the dimensionless effective potential over $y = 0$ plane. White regions correspond to $\Psi > -0.6$, black regions $\Psi < -3$ and intermediate gray levels $\Delta\Psi = 0.15$. Lines correspond to fields lines with summit of $\gamma = \sqrt[3]{2/3}$ (solid), $\gamma = \sqrt{2}$ (dashed), $\gamma = 2$ (dotted), $\gamma = 4$ (dot-dashed) for the obliquity $\beta = 30°$, $\beta = 60°$ and $\beta = 90°$ (Townsend et al., 2005).

2.2 Polarization

A beam of monochromatic light is electromagnetic radiation of any wavelength. It is composed of an electric field and a magnetic field perpendicular to each other oscillating with frequency ν. Assuming a beam of light propagating in the z axis of a coordinate system, such an electric field can be represented by two components:

$$\vec{E}(z,t) = E_x\hat{x} + E_y\hat{y} \tag{2.3}$$

in which

$$\begin{cases} E_x = \epsilon_x e^{i\varphi_x} e^{i2\pi(z/\lambda - \nu t)}, \\ E_y = \epsilon_y e^{i\varphi_y} e^{i2\pi(z/\lambda - \nu t)} \end{cases} \tag{2.4}$$

where ϵ_x and ϵ_y are the amplitudes of each component of the electric field and φ_x and φ_y are their phases. λ is the wavelength, $\lambda = c/\nu$, c is the speed of light.

A beam of light is said to be polarized when the electric field component of a beam

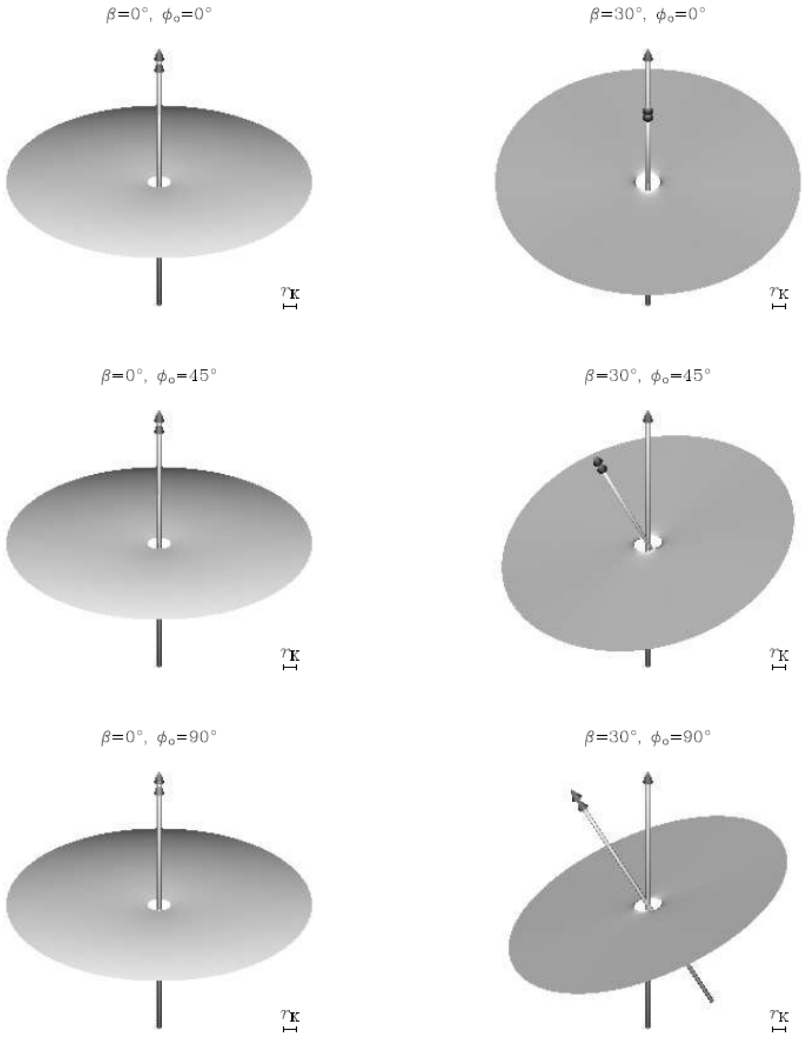

Figure 2.2: Accumulation surface for a aligned magnetic field $\beta = 0$ (left) and tilted $\beta = 30°$ (right) viewed at inclination $i = 60°$ and from azimuth (top to bottom) $\phi = 0$, 45° and 90°. The rotation axis is the single-head arrow and the magnetic field is the double-head arrow, respectively. The bar is the length of one Keplerian corotation radius (R_K).

of light oscillates in a specific orientation. The polarization of light can be classified into three groups:

- Linear Polarization: if the components E_x and E_y are in phase or anti-phase (i.e., $\varphi_x - \varphi_y = n\pi$, $n \in \mathbb{Z}$), it is said that the light is linearly polarized. The orientation of the polarization is determined by the amplitudes ϵ_x and ϵ_y and is defined by $\theta = \arctan(\epsilon_y/\epsilon_x)$.

- Circular Polarization: if the components have the exact same amplitude and are out of phase at 90° or 270° (i.e., $\epsilon_y = \epsilon_x$ and $\varphi_y - \varphi_x = (n + 1/2)\pi$, $n \in \mathbb{Z}$) the beam is circularly polarized.

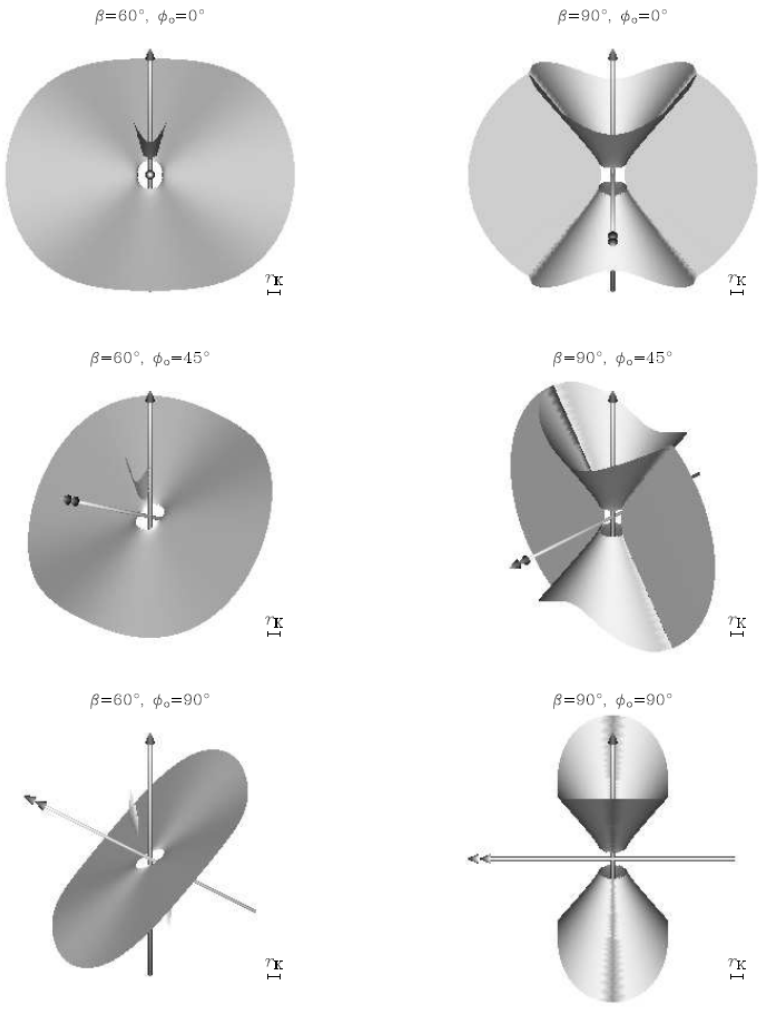

Figure 2.3: Same as Fig. 2.2, for $\beta = 60°$ (left) and $\beta = 90°$ (right).

- Elliptical Polarization: any other combination of values for the amplitudes of each component and difference in phase, the beam is a combination of linear and circular polarization. In this case, the beam is called elliptically polarized.

The polarization angle indicates the orientation of vibration of the electric field and not the direction. The angle is then graduated from 0 to 180°, since θ and $\theta \pm 180°$ refers to the same orientation.

2.2.1 Stokes Parameters

The polarization of the light is usually represented by a set of parameters, as proposed by Stokes (1851), called Stokes parameters. There are four parameters, namely $\mathcal{I}$, $\mathcal{Q}$, $\mathcal{U}$, $\mathcal{V}$, and they are represented mathematically by the equations

$$\begin{aligned}
\mathcal{I} &= E_x E_x^* + E_y E_y^* & \mathcal{I} &= \epsilon_x^2 + \epsilon_y^2 \\
\mathcal{Q} &= E_x E_x^* - E_y E_y^* & \mathcal{Q} &= \epsilon_x^2 - \epsilon_y^2 \\
\mathcal{U} &= E_x E_y^* + E_y E_y^* & \mathcal{U} &= 2\epsilon_x \epsilon_y \cos(\Delta\varphi) \\
\mathcal{V} &= i(E_x E_y^* - E_y E_x^*) & \mathcal{V} &= 2\epsilon_x \epsilon_y \sin(\Delta\varphi)
\end{aligned} \tag{2.5}$$

where the symbol $*$ is the complex conjugate and $\Delta\varphi = \varphi_y - \varphi_x$.

The parameter $\mathcal{I}$ is proportional to the total intensity of the radiation since the energy of an electromagnetic wave is proportional to $\langle \|\vec{E}\|^2 \rangle = \frac{1}{2}\epsilon_x^2 + \frac{1}{2}\epsilon_y^2$. The other three parameters are proportional to the difference in the intensity of each polarization component of the light (see Fig. 2.4).

In general, the polarization of a beam of light can be represented by an ellipse that demarcates the orientation of the electric field vector as the wave propagates (Fig. 2.5). Instead of ϵ_x, ϵ_y and $\Delta\varphi$, we can use θ and χ – the polarization angle and the angle associated to the "eccentricity" of the polarization. We can rewrite Eqs. 2.5 using these two variables, along with $\epsilon_0^2 = \epsilon_x^2 + \epsilon_y^2$:

$$\begin{aligned}
\mathcal{I} &= \epsilon_0^2, \\
\mathcal{Q} &= \epsilon_0^2 \cos(2\chi)\cos(2\theta), \\
\mathcal{U} &= \epsilon_0^2 \cos(2\chi)\sin(2\theta), \\
\mathcal{V} &= \epsilon_0^2 \sin(2\chi,)
\end{aligned} \tag{2.6}$$

so that:

$$\theta = \frac{1}{2}\arctan\frac{\mathcal{U}}{\mathcal{Q}}, \tag{2.7a}$$

$$\chi = \frac{1}{2}\arcsin\frac{\mathcal{V}}{\mathcal{I}}. \tag{2.7b}$$

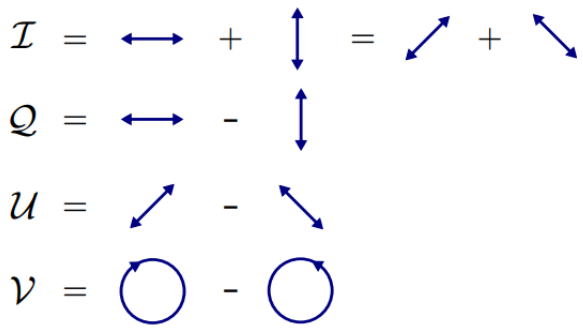

Figure 2.4: Geometrical interpretation of the Stokes parameters. Each arrow indicates the direction in which the electric field is oscillating.

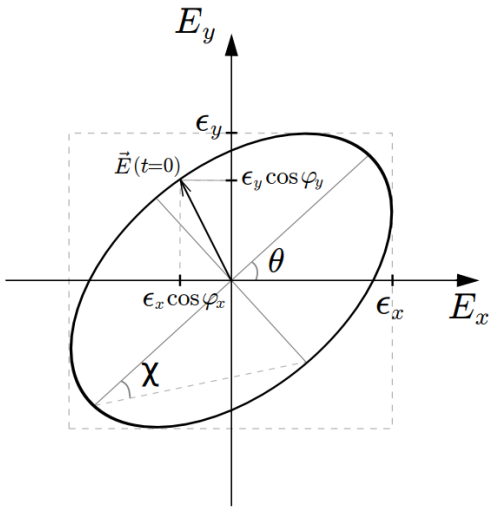

Figure 2.5: Elliptically polarized beam decomposed in the E_y and E_x components. The ellipse demarcates the position of the electric field vector as a function of time at $t = 0$. If $\chi = 0$, the polarization is linear, if $\chi = 45°$, the polarization is circular.

2.2.2 Linear Polarization

In this work, we are investigating magnetospheres utilizing their linear polarization, which is derived by the $\mathcal{Q}$ and $\mathcal{U}$ Stokes parameters. It is usual to write the parameters as a fraction of the total intensity $\mathcal{I}$ of the light. Defining $Q = \mathcal{Q}/\mathcal{I}$ and $U = \mathcal{U}/\mathcal{I}$, the percentage of linearly polarized light and the angle of polarization are:

$$P = \sqrt{Q^2 + U^2}, \tag{2.8a}$$

$$\theta = \frac{1}{2} \arctan \frac{U}{Q}. \tag{2.8b}$$

If the Stokes parameters Q and U have the same error (σ_Q), the uncertainty σ_P of the

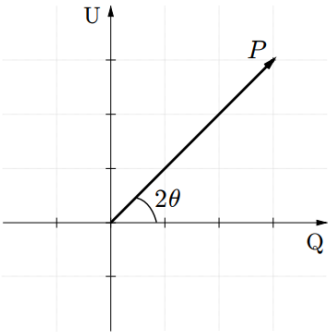

Figure 2.6: Representation of a beam with polarization P and angle of polarization θ in the QU diagram.

polarization P and θ is (Serkowski, 1974):

$$\sigma_P = \sigma_Q, \tag{2.9a}$$

$$\sigma_\theta = \frac{90}{\pi}\frac{\sigma}{P} \approx 28.65\frac{\sigma}{P}. \tag{2.9b}$$

The polarization can be represented by a vector[1] in a QU diagram (see Fig. 2.6). The magnitude of the vector is the percentage of the linearly polarized light and the angle of polarization is twice the angle from the origin $Q = 0$ and $U = 0$.

For astronomical applications, it is necessary to define a system of reference for the direction of the electric field in the plane of the sky. The International Astronomical Union (IAU) agreed to the usage of the equatorial system, where the angle of polarization is measured from north to the east in the sky (anticlockwise) (Hamaker et al., 1996).

2.2.3 Polarization bias

Representing the polarization using P and θ can give rise to a bias in the polarization. If the real value of the Stokes parameters Q and U of a beam is zero, the polarization P must also be compatible with zero. However, due to intrinsic systematic errors in the process of measuring the Stokes parameters, Q and U will have non-null values. The degree of polarization P will then be overestimated since the equation will amplify this value.

[1] Technically it is a pseudo-vector, but for simplicity, we will use the term vector from now on.

Corrections utilizing $P \rightarrow \sqrt{P^2 - K^2\sigma_P^2}$, with σ_P being the error of P, have been proposed by several works, with different values for the correction factor K.

To discriminate the best value for K it is necessary to have some previous knowledge about the polarization of the target, or an idea of its value. Since in this work we are dealing with very low values for the polarization, and the values are not previously known, we adopted $K = 1.0$, as proposed by Wardle and Kronberg (1974). This value is preferable in most cases and is the most commonly used in literature.

The error of the polarization angle is also biased when the polarization is compatible with zero (see Eq. 2.9) - as P is overestimated, σ_P is underestimated. In this case, the correction was proposed by Maier et al. (2014) through Bayesian analysis, fitting analytic functions over the curves of the confidence interval of the angle of polarization.

The polarization P and the error of polarization angle σ_θ after the correction, are:

$$P \rightarrow \begin{cases} \sqrt{P^2 - K^2\sigma_P^2} & \text{, if } P/\sigma_P \geq K \\ 0 & \text{, if } P/\sigma_P < K \end{cases} \tag{2.10a}$$

$$\sigma_\theta \rightarrow \begin{cases} \sigma_\theta & \text{, if } P/\sigma_P \geq 6 \\ 32.5\left[1.35 + \tanh\left(0.739\left(0.801 - \frac{P}{\sigma_P}\right)\right)\right] - 1.154\frac{P}{\sigma_p} & \text{, if } P/\sigma_P < 6 \end{cases} \tag{2.10b}$$

The polarization P in Eq. 2.10b is related to the *observed* polarization, and not to the one corrected in Eq. 2.10a

2.2.4 Interstellar Polarization

While searching for intrinsic polarization in OB stars, Hall (1949) and Hiltner (1949) noticed a clear coherent pattern of position angles across the sky in several directions in the Milky Way. The pattern could not be due to the intrinsic polarization of the stars, since their rotation axes are likely to be randomly distributed over the sky. Since there was a clear positive correlation between polarization and extinction, the polarization was attributed to the presence of asymmetric grains that are aligned with the Galactic magnetic field (Serkowski et al., 1975).

The light becomes polarized when a beam of unpolarized light in the optical range is partially absorbed by an elongated grain of dust. The absorption will be more intense along the major elongation axis of the grain, thus producing a net polarization when the grains

are highly elongated. The presence of a local galactic magnetic field causes the grains to have a preferred direction of alignment in the sky, causing the light to be partially polarized in the perpendicular direction of the grains. Without the presence of the local magnetic field, the grains would be randomly distributed and the net polarization would be zero (Lazarian, 2003).

The study of linear and circular polarization is important because they provide information on the galactic magnetic field and also on grain properties, such as their size, shape, and refractive index. However, it may cause a negative effect in the study of the intrinsic polarization of OB stars, since it affects not only the degree and angle of polarization but also the behavior of the observed temporal variability. Therefore, measuring interstellar polarization is of utmost importance.

2.2.5 Thomson scattering

Thomson scattering is an important phenomenon in plasma physics and was first explained by Thomson (1906). It is the scattering of light off a *non-relativistic* charged particle that is accelerated by the electric field of the incident radiation, causing it to emit radiation at the same frequency but in different directions. The moving particle will radiate most strongly in a direction perpendicular to its acceleration (see Fig. 2.7) and that radiation will be polarized along the direction of its motion.

In a perfectly symmetrical stellar envelope and also in stellar photospheres, the local polarization created by Thomson scattering will be canceled by the polarization on the opposite side of the envelope, and, in that case, the intrinsic net polarization will be null. However, if the envelope is not perfectly symmetrical, this net canceling will not happen and the intrinsic polarization is non-null (Fig. 2.8). In this case, the resulting polarization will be perpendicular to the plane of scattering of the particles.

Thus, in the case of an electron-rich circumstellar environment – common in many types of OB stars such as Be stars, O stars, etc. – polarimetry is a powerful tool that allows one to obtain the shape, density, and direction of the envelope in the plane of the sky. This has been done frequently for Be stars (e.g. Klement et al., 2015; Carciofi et al., 2009). For the subject of this MSc dissertation, we expect that polarimetry is also a powerful diagnosis of the magnetosphere of massive stars.

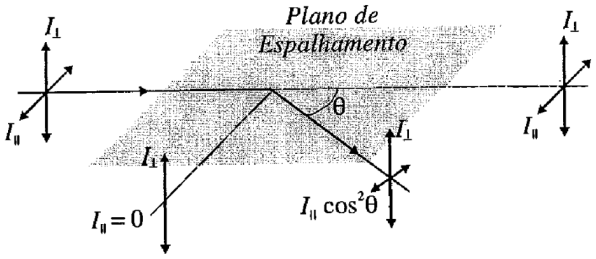

Figure 2.7: Representation of Thomson scattering at angle θ. The percentage of polarized light after being scattered is given by $P = (1 - cos^2(\theta))/(1 + cos^2(\theta))$. The direction of the polarized beam will always be perpendicular to the scattering plane, except for $\theta = 0$ or $\theta = 180°$, in which the polarization will remain zero. The intensity of the electric field parallel ($I^{\parallel}$) to the scattering plane always decreases, while the perpendicular component ($I^{\perp}$) does not change (Carciofi e Magalhães, Carciofi and Magalhães).

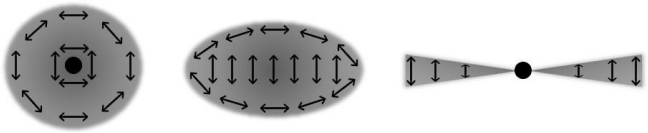

Figure 2.8: Polarization vectors of the circumstellar material after being Thomson scattered. In a symmetrical envelope, the polarization of each individual scattering will cancel out each other and the net polarization is zero. For a disk-like structure, the polarization does not cancel each other and the net polarization is perpendicular to the disk. Courtesy of A. C. Fonseca Silva

2.3 Dumbbell plus Disk Model

2.3.1 Motivation

The BeAcON group has an ongoing survey of high-precision polarimetry of magnetic hot stars since 2010. In 2013, Carciofi et al. (2013) reported the first firm detection of a hot star magnetosphere in continuum linear polarization.

The authors tried to reproduce the observed polarization modulation of σ Ori E by feeding the predicted density distribution of the RRM model to the HDUST radiative transfer code. They could not find a model that can reproduce both the photometry and polarimetry of σ Ori E simultaneously (Fig. 2.9).

A higher density model (solid line) that matches the eclipses present in the photometry predicts an amplitude in the polarization that is three times higher than the observed. Alternatively, a lower-density model (dotted line) that is capable of reproducing the ampli-

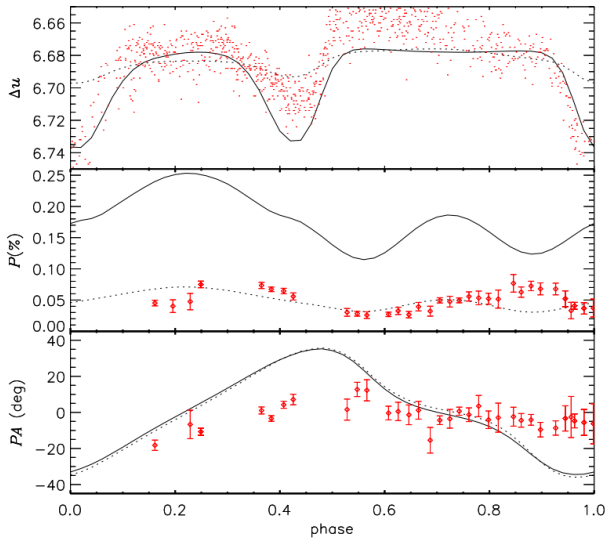

Figure 2.9: Modeling the observed (red) intrinsic polarization of σ Ori E using the RRM model. The only free parameter is the maximum number density in the magnetosphere. A model with a higher density of 10^{12}cm^{-3} was set to match the eclipses present in the photometry (solid lines) and a lower density of 2.5×10^{11}cm^{-3} to reproduce the amplitude of the linear polarization (dotted lines). Top: photometry of σ Ori E. Middle: observed intrinsic polarization. Bottom: Angle of polarization. Both models fail to reproduce the observed polarization angle (Carciofi et al., 2013).

tude of the polarization fails to reproduce the photometric amplitude. Furthermore, both models fail to reproduce the modulation of the polarization, in particular the polarization angle.

Since the angle is sensitive to the geometry of the scattering material. The discrepancy present in the polarization led the authors to conclude that although the RRM model does predict the structures present in σ Ori E magnetosphere, the relative masses of these structures are incorrectly predicted by the model.

2.3.2 Single scattering model

Based on the RRM model, Carciofi et al. (2013) developed a simple, parametric ad-hoc model that consists of a thin uniform disk tilted by an angle β from the rotational axis and a pair of spherical blobs situated at the intersection between the equatorial plane and the magnetic equator (Fig. 2.10). This configuration mimics a dumbbell shape and was named *Dumbbell plus Disk* (hereafter, D+D model).

Since the polarization is small, the Q and U Stokes parameters can be determined by the model as a function of orbital phase for a given inclination angle i following a simple single-

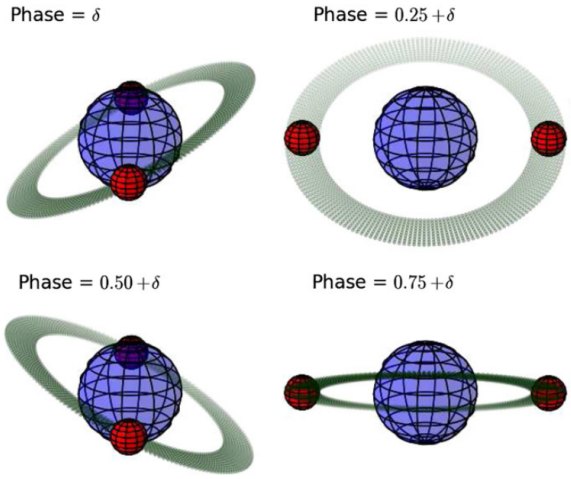

Figure 2.10: Geometric conception of the Dumbbell plus Disk model ($i = 70°$). δ indicates the phase shift between the photometric and polarimetric minima (Carciofi et al., 2013).

scattering approach (valid only in the optically thin limit) through Thomson scattering. The scattered flux is determined first in the frame of the star using the formalism described by Bjorkman and Bjorkman (1994, Eq. 6) and then rotated to the frame of the observer (Bjorkman and Bjorkman, 1994, Eq. 20).

Initially, Carciofi et al. (2013) adopted five fixed parameters and seven free parameters (see Table 2.1). The fixed parameters were adopted from the models of Townsend and Owocki (2005), and are $R_\star$, the star radius, d_b, the distance of the blobs from the star, R_b, the size of the blobs, H_d, the geometrical thickness of the disk and i, the inclination angle. It is important to note that the radius of the spherical blobs R_b is somewhat arbitrary: in a single-scattering approximation and in the limit $R_b < R_\star$, a large, tenuous blob is equivalent to a small, dense blob. The same logic applies to the disk: if the single-scattering approximation holds, a denser, small disk is equivalent to a less dense, thicker disk. In other words, what really controls the polarization level of each component is the total mass of scatterers and not the details of their geometry.

The criteria used to define the geometrical configuration of the D+D model are:

- The stellar radius adopted is the equatorial radius ($R_\star = R_{eq}$)
- The center of the blob is at R_K, the Keplerian corotation radius.
- The blobs diameter is fixed at $2/3R_\star$.
- The polarimetric period adopted is the same as photometry and spectroscopy.

Table 2.1 - Parameters of the D+D routine and the best fit for σ Ori E.

Parameter	Type	Best fit
i (deg)	Fixed	70
$R_\star(R_\odot)$	Fixed	3.1
$d_b(R_\star)$	Fixed	2.4
$R_b(R_\star)$	Fixed	2/3
$H_d(R_\star)$	Fixed	0.01
n_e^b	Fitted	$1.0^{+0.6}_{-0.9} \times 10^{12}$
n_e^d	Fitted	$2.7 \pm 1.0 \times 10^{12}$
α (deg)	Fitted	28
Q_{IS} (%)	Fitted	-0.35 ± 0.01
U_{IS} (%)	Fitted	0.025 ± 0.010
Θ (deg)	Fitted	150
δ	Fitted	0.085 ± 0.02

- The disk (rather, a ring) component has the same radial position and size as the blob, with a fixed scale height of $H = 0.01 R_\star$.

The free parameters of the D+D model are, as adopted by Carciofi et al. (2013): n_e^b, the electron density of the blobs, n_e^d, the density of the disk, Q_{IS} and U_{IS}, the Q and U Stokes parameters of the interstellar polarization, Θ, the position angle of the equatorial plane in the plane of the sky, δ, the phase lag between the photometric primary minimum and the orbital phase where the blobs are aligned with the line of sight and β, the obliquity of the magnetic field. In their code, the obliquity is set by the complementary angle $\alpha = 90^\circ - \beta$ shown in the figures.

Some of the fixed parameters (i, $R_\star$, and d_b) were obtained from the literature. The latter was obtained from $H\alpha$ monitoring of the magnetospheric emission, which allows mapping the location of the emission in velocity space. The translation to physical distance is possible because the rotation rate of the star is known. The other parameters (R_b and H_d) can be loosely estimated by the same process. However, it is important to notice that, since the magnetospheres are quite optically thin, the only quantity that can be unambiguously determined from polarimetry is the total mass of scatters (i.e., free electrons). Hence, the combination of n_e^b, n_e^d, R_b and H_d is degenerate, in the sense that there are infinite combinations of these four parameters that have the same total e^- mass. This justifies

our choice for fixing a pair of parameters and fitting the other pair. The fitted parameters are divided into two groups: the parameters related to the magnetosphere, intrinsic to the star, and the parameters related to the interstellar polarization, not intrinsic to the star. The D+D model is described in detail in Carciofi et al. (2013). The best-fitted parameters are in Table 2.1

The interstellar polarization obtained by the model was consistent with the measurements of σ Ori AB. With the best-fitting parameters, the authors estimated the mass of the blobs, $M_b = 6.0 \times 10^{-12} M_\odot$, and disk $M_d = 1.0 \times 10^{-11} M_\odot$. Both components of the model have approximately the same mass ($2M_b/M_d = 1.2$).

Fig. 2.11 shows the polarization after the correction of the interstellar polarization of Table 2.1. The two minima of the polarization occur when the blobs are aligned with the line of sight ($\phi \approx \delta$ and $\phi \approx \delta + 0.5$), while the maxima occur when the blobs are on the side of the star ($\phi \approx \delta + 0.25$ and $\phi \approx \delta + 0.75$).

Another interesting result is that the model was able to distinguish the rotational direction of the star in the sky. The solid curves of Fig. 2.11 correspond to the best-fitting model for $i = 70°$, and the dashed curves to the best-fitting model for $i = 110°$. The former has a much better fit to the data.

The main conclusion of Carciofi et al. (2013) is that, although the RRM model of Townsend et al. (2005) does predict the structures present in σ Ori E's magnetosphere (namely a tilted disk and two blobs), the relative masses of these structures are incorrectly predicted by the model. This discrepancy indicates that the RRM must be further developed in order to successfully describe the magnetosphere around massive stars with very strong magnetic fields.

2.3.3 New D+D Analysis

The fit of the D+D model presented by Carciofi et al. (2013) was performed manually, by changing the parameters around a χ^2 minimum that was found by computing a model grid.

In this work, we present a new approach to the D+D model adopting a more robust statistical treatment than used before. We utilize Bayesian statistics via the Markov Chain Monte Carlo method, such as described in Section 2.4, that will allow a much more precise fitting of the D+D model to the data. The minimization simultaneously determines all the

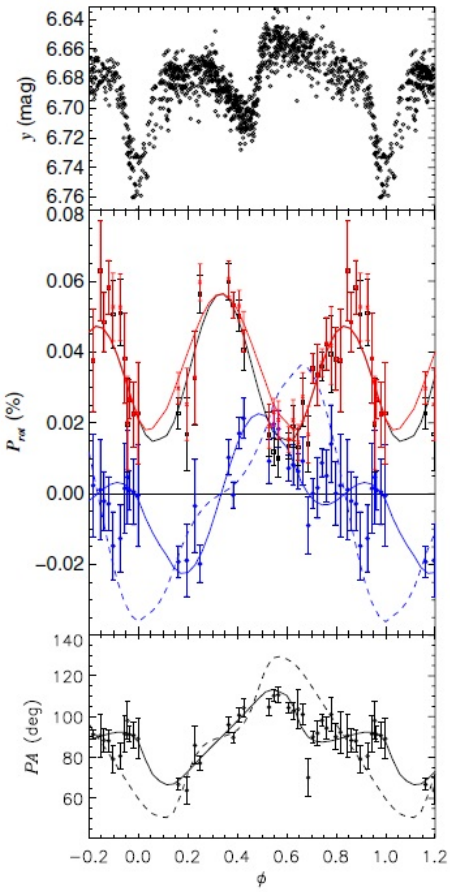

Figure 2.11: Top: photometry of σ Ori E showing the two eclipses created by the clouds that corotate the star. Middle: linear polarization (red) of the star. Black and blue are the Q and U Stokes parameters. Bottom: angle of polarization. Solid line is the D+D model for $i = 70°$, dashed line is $i = 110°$. Image adapted from Carciofi et al. (2013).

selected physical parameters involved in the modeling. This method allows the evaluation of the correlation between the parameters and the uncertainty in their determination, in a self-consistent analysis. Similar work was done by Faes (2015), where they present preliminary results of their routine.

In the new routine of the D+D, it is also possible to select which parameters will be modeled and which will be fixed. Running the simulation several times for different combinations of fixed and free parameters allows for studying the behavior of the results and how a parameter may affect the others. It is important to note that a parameter can only be fixed if we know its "true" value if it is available from the literature.

2.4 emcee

Foreman-Mackey et al. (2013) presented an efficient open source code of the Markov Chain Monte Carlo (MCMC) method, which is used to fit models to observations and estimate each parameter posterior probability using the Bayes theorem. `emcee` is an ensemble MCMC algorithm, it does not consider a single Markov Chain, but multiple chains where the next step in each chain depends on the value of the previous position of the chain. This characteristic is translated in the code by the walkers variable, chosen by the user, which determines how many "Markov Chains" the code will use to sample the problem given.

The great advantage of using this method instead of obtaining just the best-fit model, as we would do from the frequentist approach, is that we find a distinct probability density function for each of the parameters, and the correlations between them.

It is important to note that, since the MCMC is inherently Bayesian, it requires us to impose what is known as *priors* on our parameters. Priors are any previous knowledge that we have about our parameters; it can be, for example, a fixed value with a Gaussian error distribution or a range that the value must be contained in.

In the frame of this work, for each model (or a set of parameters randomly generated in the MCMC simulation) the following steps are performed:

1. The intrinsic polarization model is generated in the stellar reference system for all rotational phases

2. The model is rotated to the equatorial system. It is important to distinguish between clockwise and counter-clockwise rotation. This is done by having i as a free parameter ranging from 0 to 180 degrees.

3. Interstellar polarization components Q_{IS} and U_{IS} are randomly sampled within a predetermined interval. The interval is determined by field star analysis, if available. The interstellar polarization is then added to the intrinsic polarization.

4. The χ^2 value is computed to determine the likelihood associated with model parameters. The higher the likelihood, the lower χ^2, defined as

$$\chi^2 = \sum_i^N \left[\frac{Q_{\rm obs}\left(\phi_i\right) - Q_{\rm mod}\left(\phi_i\right)}{\sigma_{Q(\phi_i)}} \right]^2 + \sum_i^N \left[\frac{U_{\rm obs}\left(\phi_i\right) - U_{\rm mod}\left(\phi_i\right)}{\sigma_{U(\phi_i)}} \right]^2 \tag{2.11}$$

5. Based on the likelihood of the current parameters, a new set is generated until reaching the number of iterations defined by the user.

2.4.1 Corner plots

One advantage of Bayesian statistics using the emcee algorithm is the corner plots. The corner plot is an illustrative representation of different projections of samples in high-dimensional projections. It shows all the one and two-dimensional projections of the posterior probability distribution of the parameters and is useful because it quickly demonstrates all of the covariances between parameters. Essentially, the corner plot shows the marginalized distribution for each parameter independently in the histograms along the diagonal and then the marginalized two-dimensional distribution in the other panels. Examples of corner plots are shown later in this manuscript (e.g. Fig 4.4).

2.4.2 Probability Density Function

At the end of the process, we have what is known as posterior distribution or chain. Every walker keeps a record of every set of parameters that it tried out, and the likelihood of the model given the data in the values of the parameters. It is important to remember that MCMC is not a "fitter", it is a "sampler". Assuming the MCMC runs long enough to converge reasonably, the distribution represents a sample of reasonable models to describe the data.

Chapter 3

Observational Data

3.1 Polarimetic Survey of Magnetic Stars

The BeACoN group, led by Prof. Dr. Alex C. Carciofi has an ongoing polarimetric survey of Be and magnetic OB stars at Observatório Pico dos Dias (OPD) since 2010. The observatory is managed by Laboratório Nacional de Astrofísica (LNA/MCTI) and is located in Brasópolis-MG.

The telescopes used in the survey were the 60 cm *Boller & Chivens* (B&C) and *Zeiss*, and the 1.6 m *Pelkin-Elmer* telescopes. The most used in this survey was the B&C telescope. Until July 2022, the project was granted 633 nights, in which 115 Be stars and 18 magnetic OB stars were observed. While conducting this MSc project, we were granted extra 34 nights to monitor the linear polarization of magnetic OB stars; 10 of these nights were in the *Pelkin-Elmer* telescope.

3.1.1 IAGPOL polarimeter

As seen in Section 2.2, a beam of polarized light has the electric field component oscillating in a specific direction. The instrument used to detect the direction and polarized percentage of the total intensity is called *polarimeter*.

The polarimeter used in the missions at OPD is named IAGPOL (Magalhães et al., 1996). It consists of a half-wave plate to measure the linear polarization and an analyzer that can be either a Savart prism made of calcite or a polaroid. The incident beam of light first passes through the wave plate, which adds a 180° phase lag to the components of the electric field parallel and perpendicular to the optical axis of the plate. It is possible to rotate this optical axis in 16 different angular positions, in steps of 22.5°. The role

of the wave plate in creating a phase lag of the electric field components is to effectively rotate the original polarization of the observed object, making projections of the distinct components of the polarization on the optical axis of the analyzer.

Then the beam passes through the analyzer, which in our case is a Savart prism made of calcite. Calcite is a birefringent material, which means that its refractive index depends on the orientation of the electric field. When the beam of light hits the calcite, it refracts two electromagnetic components of the light at different angles, physically separating them into the so-called ordinary beam (OB) and extraordinary beam (EOB). In the case of a polarized incident intensity, there will be a modulation of the two beams as the half-wave plate rotates. Measuring this modulation is the main task of the polarimeter.

The two beams of light then pass through a UBVRI filter wheel, through which the spectral region of interest is selected and are finally recorded by a *charged-coupled device* (CCD) detector.

Once the intensity of the ordinary beam ($I_{\rm OB}$) and extraordinary beam ($I_{\rm EOB}$) are registered in several positions of the wave plate, it is possible to effectively map how the difference in the intensity of the light varies at different directions of the electric field oscillation i.e., how the position of the wave plate modules the linear polarization of the target. The polarization can be represented with the Stokes parameters Q and U (Serkowski, 1974; Magalhaes, 2012):

$$p \equiv \frac{I_{\rm OB} - I_{\rm EOB}}{I_{\rm OB} + I_{\rm EOB}} = Q\cos(4\phi) + U\sin(4\phi), \tag{3.1}$$

where ϕ is the angle between the optical axis of the wave plate and the calcite. The wave plate is rotated from north to east, following the equatorial system. However, the projected direction of the optical axis of the calcite in the sky will set the reference polarization angle $\theta = 0$.

In this situation, observations with the wave plate at specific positions will give us the Q and U Stokes parameters directly:

$$p(0.0^\circ) = Q;$$
$$p(22.5^\circ) = U;$$
$$p(45.0^\circ) = -Q;$$
$$p(77.5^\circ) = -U;$$

In practice, we do not know the angle θ, as it depends on how the polarimeter was built. Thus, to determine it, we observed standard stars, whose polarization angles are known. As the position of the calcite optical axis changes with the wavelength, these observations must be done in each filter.

It is usual to observe stars at least in 8 positions of the wave plate instead of only 2 to determine the Q and U Stokes parameters through Eq. 2.5. At each position the total exposure time is distributed over several images to be summed during reduction, resulting in a reasonable signal-to-noise (S/N).

3.1.2 Field Stars

One of the free parameters of the D+D model is the interstellar polarization (ISP). It is a relevant parameter in understanding the intrinsic polarization of the magnetosphere, as well as its modulation. One method of determining the ISP is through field stars. This method is performed by observing stars that are physically close to the target star we want to study. Assuming the field stars do not have intrinsic polarization, then the polarization observed is attributed to the interstellar medium. And since the field stars are close to the magnetic star, they should have the same ISP. In practice, the ISP level depends on the amount of intervening interstellar material. Therefore, ideally one should observe several (3 or more) field stars to map how ISP level varies with distance, and then use this information to estimate the ISP at the target's location. Clearly, this task is now much more facilitated given the precise distances from Gaia mission (Prusti et al., 2016).

The closer the field stars are to the target, either in distance or angle or both, they are more likely to be in the same interstellar medium and the ISP field can be determined more precisely. One important usage of the ISP is to compute the intrinsic polarization of the target star. If different than zero, it would be a direct detection of the magnetosphere (one

of the primary goals of this project). Another important way is to adopt this information as prior to the MCMC routine, allowing it to model more efficiently.

The above shows that the ISP is a piece of crucial information, and that is why a great effort was made in this project to observe field stars. This was done in collaboration with MSc student Ariane Cristina Fonseca Silva.

3.1.3 Data Reduction

The data reduction process computes the Q and U Stokes parameters from the raw images of the observed objects. It is done through a software named IRAF (*Image Reduction and Analysis Facility,* Tody, 1993) using the BEACON[1] package. The contributors to the current version of the BEACON package are Alex C Carciofi, Antônio Mário Magalhães, Antonio Pereyra, Daniel Bednarski Ramos, and Daniel Moser Faes. The reduction of the data of all magnetic stars observed since 2016 was made by Ariane Cristina Fonseca Silva. Prior to this date, it was mostly done by MSc Daniel Bednarski Ramos.

The BEACON package has many routines that facilitate the above process, in order to handle several observations of many targets. The routines are listed below:

- `zerocombine`: Make an average image of the bias images acquired in the observations;
- `ccdproc`: subtracts the bias images from each flat image;
- `flatcombine`: creates an average flat image from the images corrected by the `ccdproc` task.
- `ccdrap`: calculates the ordinary and extraordinary beam photometry for each wave-plate position
- `polrap`: uses the photometry results to calculate polarization modulation for each wave-plate position.

The data reduction starts with the treatment of calibration images. First, an average of the *bias* images is created from the sequence of acquired images. The resulting image is subtracted from the corresponding *flat* field images. These, in turn, are summed up and normalized by average counts, resulting in a final flat image for each filter.

[1] Available at https://github.com/danmoser/beacon

The next step is to reduce the data of each observed target. Initially, the images are processed so that bias and flat field corrections are applied. Then, for each wave-plate position, all images are aligned (using IRAF tool `imalign`) and stacked (`phot` routine). Then, an aperture photometry is performed on both the OB and the EOB beams. Sky subtraction is also performed in this step. This returns a file with the photon count of the ordinary and extraordinary beams and their uncertainties, at each wave-plate position.

The next step is to calculate the component $p = (I_{\rm OB} - I_{\rm EOB})/(I_{\rm OB} + I_{\rm EOB})$ of the polarization of the star at each wave-plate position using the routine `ccdrap`. Finally, Eq. 3.1 is fitted to the table p vs. ϕ through `polrap`, thus producing the value Q and U, from which the total polarization and polarization angle are calculated. The process above is carried out for several aperture masks, typically ranging from 3 to 12 arcsec. The final values for the Stokes parameters will be those with the lowest error. Fig 3.1 illustrates the complete process of data reduction. After the curating process, the file `star.log` contains the observed Q and U Stokes parameters and the angle of polarization along with its errors and filters used.

3.2 Sample

We created our sample of stars by searching in literature for stars with strong magnetic fields. We also looked for magnetic stars with rotation periods short enough to potentially be able to support a centrifugal magnetosphere. Stars with larger rotation periods (thus not able to support a centrifugal magnetosphere) were not excluded from the survey but were given a lower priority in the observing list. At the beginning of this MSc dissertation, the BeACoN survey had 13 magnetic OB stars in their list, but most of them with a patchy phase coverage. Today, the number of stars on our list has increased to 27. The stars are listed in Table 3.1.

Of all the 27 magnetic stars in our list, we have polarimetric data of 18 of them. The stars for which we already started the polarimetric monitoring at OPD are listed in Table 3.2. The stars were mostly observed in the V and R bands, but for some of them we only have data in the V band. The polarimetric data of HD 35502 was provided by Andrei Berduygin and Vilppu Piirola during an observing run between November and December of 2015. The polarimetric data of σ Ori E is the same of Carciofi et al. (2013). The disparity

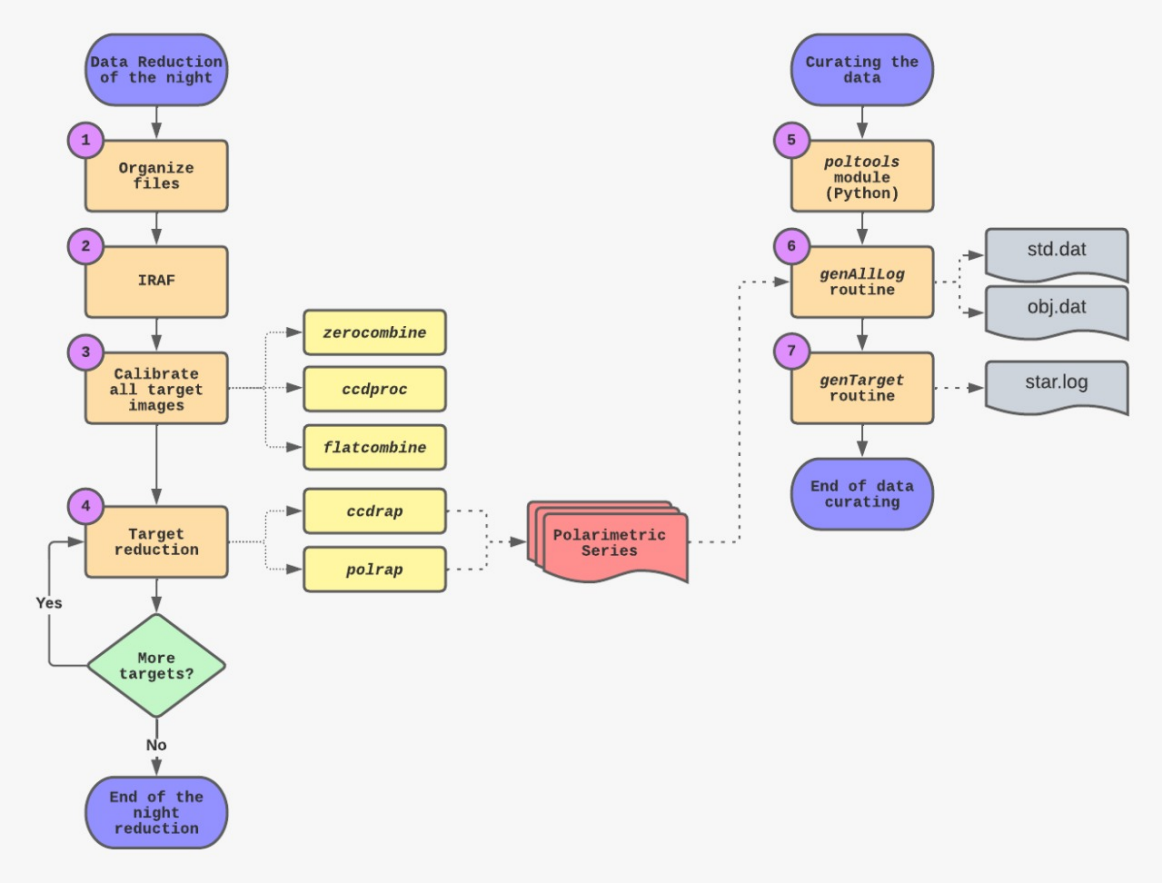

Figure 3.1: Illustration of the data reduction process. After the calibration, the `ccdrap` and `polrap` routines return the Q and U Stokes parameters fitted using Eq. 3.1. After the curating process, the file which contains the observational data is `star.log`.

in the number of nights with observations of HR 5907 and HR 7355 is because the BeACoN group has started the polarimetric monitoring of these stars in 2010, while the other stars were added to the list in the last few years. Table 3.2 also shows the magnetic field strength and rotation period for all the stars we are monitoring. These are the main parameters that indicate if the star can sustain a magnetosphere.

3.2.1 Effective Planning of the Observations

For a more precise detection of the magnetosphere and to reliably model it with the D+D model, it is necessary the linear polarization of the target during its complete rotation period. To optimize our telescope time, we developed a new routine that does the following: given the ephemeris (T_0 in Table 3.2) and the rotation period of the star, along with the intervals of the rotation phase that we already have covered, the script identifies the

Table 3.1 - List of the magnetic stars in our survey.

Stars		
HD23478	σ Lupi	HD35298
δ Ori C	HD96446	HD35502
θ_1 Ori C	HD148937	HD35912
HD191612	HD151018	HD36526
HD37776	τ Sco	HR1890
HD57682	HD345439	HD55522
HD64740	HR7355	HD61556
HR5907	σ Ori E	HD142990
HD306795	HD105382	HD175362

best observing nights and the optimal observing period of each night to maximize phase coverage. This script was of great value to help us plan our observing runs. The rotational phase ϕ of each star used in our analysis was calculated using the Eq 3.2:

$$\phi = \frac{T - T_0}{P} \tag{3.2}$$

where T is the Julian Day in which the stars were observed and P its period.

Table 3.3 shows the magnetic stars with their Q and U Stokes parameters of the interstellar polarization determined by the method of the field stars. It also lists the specific stars used for each programmed target. Two magnetic stars, δ Ori C and HD 37017, have an incomplete phase coverage, but we already have the data for their field stars. σ Ori E's interstellar polarization is the same reported by Carciofi et al. (2013). The field of HR 5907 is preliminary and only has two stars so far.

Table 3.2 - Parameters of the monitored magnetic stars. [(1)] Values taken from Simbad (http://simbad.cds.unistra.fr/simbad/).[(2)]Petit et al. (2013);[(3)] Townsend et al. (2010);[(4)]Sikora et al. (2016);[5]Grunhut et al. (2011); [(6)]Oksala et al. (2010), [(7)]Leto et al. (2017);[(8)]Das et al. (2019);[(9)]Shultz et al. (2018);[(10)]Krtička et al. (2013);[(11)]Mikulášek et al. (2008);[(12)]Borra and Landstreet (1979);[(13)]Leone et al. (2010);[(14)]Wade et al. (2006);[(15)];Wade et al. (2012);[(16)]Rubinho et al. (2016);[(17)]Henrichs et al. (2012);[(18)]Hubrig et al. (2017);[(19)]Donati et al. (2006);[(20)]Grunhut et al. (2012);[(21)]Wade et al. (2011);[(22)]Neiner et al. (2012).

Star	RA(2000)[(1)]	Dec(2000)[(1)]	Spectral Type[(1)]	$R_*(R_\odot)$	$M_*(M_\odot)$	B[(1)]	V[(1)]	B_p(kG)	Period (days)	#Nights	T_0(JD)
σ Ori E	05 38 47.20	-02 35 40.52	B2Vp	3.9[(2)]	5.0[(2)]	6.38	6.46	9.6[(2)]	1.19[(2)]	14	2442778.8290[(3)]
HD 35502	05 25 01.20	-02 48 55.69	B5V	3.0[(4)]	5.7[(4)]	7.30	7.34	14[(4)]	0.85[(4)]	17	2456295.81285[(4)]
HR 5907	15 53 55.86	-23 58 41.15	B2V	3.1[(5)]	5.5[(5)]	5.35	5.40	10[(5)]	0.50[(5)]	56	2447913.694[(5)]
HR 7355	19 24 30.18	-27 51 57.39	B2Vn	3.7[(6)]	6.0[(6)]	5.89	6.01	11[(6)]	0.52[(7)]	44	2454940.830[(7)]
HD 142990	15 58 34.87	-24 49 53.36	B5V	3.1[(8)]	5.7[(8)]	4.34	5.43	4.5[(8)]	0.98[(9)]	17	2443560.066[(9)]
HD 64740	07 53 03.63	-49 36 46.95	B2V	6.3[(2)]	11[(2)]	4.40	4.63	16[(2)]	1.33[(10)]	6	2444611.859[(10)]
HD 37776	05 40 56.37	-01 30 25.86	B2V	3.8[(2)]	5.5[(2)]	6.82	6.96	15[(2)]	1.54[(2)]	7	2445724.669[(11)]
HD 37017	05 35 21.87	-04 29 39.02	B2V	3.9[(2)]	7.2[(2)]	6.43	6.56	6[(2)]	0.90[(2)]	10	2442812.23[(12)]
δ Ori C	05 32 00.41	-00 17 04.35	B2Vsn	4.5[(2)]	7.1[(2)]	6.67	6.83	10[(2)]	1.48[(2)]	7	2448298.86[(13)]
θ^1 Ori C	05 35 16.47	-05 23 22.92	O7Vp	9.9[(2)]	45[(2)]	5.15	5.13	1.1[(2)]	15.42[(2)]	4	2448833.0[(14)]
HD 148937	16 33 52.39	-48 06 40.48	O6f?p	15[(2)]	60[(2)]	7.12	6.71	1.0[(2)]	7.03[(2)]	15	2454588.67[(15)]
HD 151018	16 46 56.12	-45 53 14.31	O9Ib	—	—	9.93	9.37	—	4.5[(16)]	7	—
σ Lup	14 32 37.06	-50 27 25.77	B1V	4.8[(2)]	9.0[(2)]	4.24	4.42	0.50[(2)]	3.0[(2)]	7	2445603.65[(17)]
HD 345439	19 58 48.49	+23 05 21.56	B1V	4.3[(18)]	—	11.61	11.11	12.7[(18)]	0.77[(18)]	3	2454252.3432[(18)]
τ Sco	16 35 52.95	-28 12 57.66	B0.2V	5.5[(2)]	11[(2)]	2.56	2.81	0.20[(2)]	41[(2)]	15	2453193.0[(19)]
HD 57682	07 22 02.05	-08 58 45.77	O9.2IV	7.0[(2)]	17[(2)]	6.24	6.43	1.7[(2)]	63[(2)]	3	2453347.71[(20)]
HD 191612	20 09 28.61	+35 44 01.29	O8fpe	14[(2)]	30[(2)]	8.07	7.80	2.5[(2)]	537[(2)]	7	2453415.1[(21)]
HD 96446	11 06 05.82	-59 56 59.56	B2IIIp	4.5[(2)]	8.0[(2)]	6.57	6.69	6.5[(2)]	0.85[(22)]	17	2455704.5255[(22)]

Table 3.3 - Magnetic stars for which we have finished the field stars observation and the field stars associated with each one of them.

Star	Filters	Field Stars	Q_{IS}	U_{IS}
σ Ori E	V	σ Ori AB, σ Ori C	−0.348(15)	0.040(15)
HD 35502	B, V, R	HIP 25193, HIP 24842, HIP 26334	−0.683(11)	−0.105(11)
HR 5907	V, R	HD 142249, HD 142165	−0.372(9)	0.583(9)
HR 7355	V, R	HIP 95386, HIP 95782, HIP 95604, HIP 94825	−0.082(20)	−0.067(20)

Chapter 4

Results

In this Chapter we will present the results and current state of our survey of magnetic OB stars at OPD, showing the phase coverage of the Q and U Stokes parameters for the main stars for which we have data.

We will also discuss the results of the modeling process of the stars with complete phase coverage. The modeling was made with the new routine of the Dumbbell plus Disk model coupled with the emcee code of the Monte Carlo Markov Chain method.

With that, we divided the observed stars into three groups: 1) stars with only intrinsic polarization detected, 2) stars with modulation of the intrinsic polarization, and 3) stars with phase coverage complete enough to model their magnetosphere with the Dumbbell plus Disk model.

4.1 Sample Overview

As presented in Sec. 3.2, our survey consists of 27 magnetic OB stars, and we have data for 18 of them. In our observations at OPD, we gave priority to stars with shorter rotation periods, that sustain centrifugal magnetospheres. The phase coverage of our observed targets is in Table 4.1. The data points of the phase coverage of all stars are in Appendix A.

We have five stars with a complete phase coverage: σ Ori E, HD 35502, HD 142990, HR 5907 and HR 7355. We applied the new routine of the D+D model to their data. The results are shown below. Seven stars (HD 64740, HD 37017, δ Ori C, HD 148937, τ Sco, HD 191612, HD 96446) have a phase coverage higher than 50%, and we intend to complete their phase coverage as the OPD survey unfolds. The stars with a phase coverage of 50%

Table 4.1 - Phase coverage of the magnetic OB stars from our sample.

Star	Phase coverage	Star	Phase Coverage
σ Ori E	100%	HD 35502	100%
HR 5907	100%	HR 7355	100%
HD 142990	100%	HD 64740	60%
HD 37776	30%	HD 37017	60%
δ Ori C	60%	θ^1 Ori C	20%
HD 148937	80%	HD 151018	10%
σ Lup	50%	HD 345439	10%
τ Sco	80%	HD 57682	10%
HD 191612	70%	HD 96446	70%

or lower (HD 37776, θ^1 Ori C, HD 151018, σ Lup, HD 345439 and HD 57682), along with the remaining 9 stars in our list have a lower priority in our missions, but we also intend to obtain new data for them, given the opportunity.

4.2 σ Ori E revisited

4.2.1 Target Overview

σ Ori E is by far the most studied star of its class. The discovery of σ Ori E's magnetic field was the first evidence that early-type stars can also have a significant magnetic field (Landstreet and Borra, 1978). The presence of two circumstellar clouds situated at the intersection of the magnetic and rotational equators causes an observed modulation of its Hα line (Walborn, 1974), helium absorption line (Pedersen and Thomsen, 1977), photometry (Hesser et al., 1976), 6 cm radio emission (Leone and Umana, 1993) and polarization (Carciofi et al., 2013).

In order the verify the new routine of the D+D coupled with the emcee code, we did a reanalysis of the observational data of σ Ori E. Fig. 4.1 shows the intrinsic polarization (observational data subtracted by the interstellar polarization) with the best fit found by our model. The model fits very well both the Q and U Stokes parameters. The polarization P and the angle of polarization θ were calculated using Eqs. 2.9a and 2.9b.

Table 4.2 compares the values of the best parameters of the magnetosphere found by our new model to the results of Carciofi et al. (2013). The priors of $Q_{\rm IS}$ and $U_{\rm IS}$ were taken

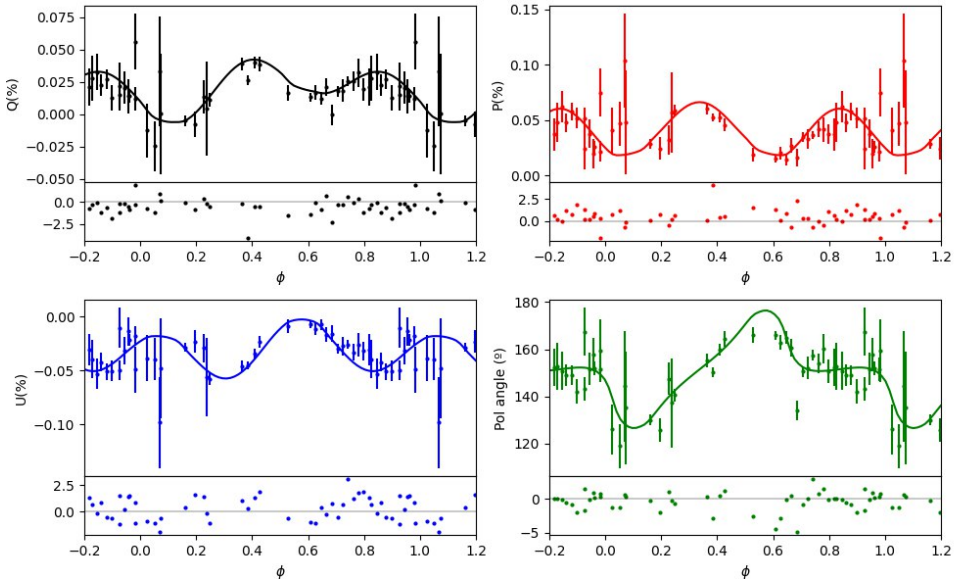

Figure 4.1: Intrinsic polarization of σ Ori E with the best fit found by the D+D model. Q and U Stokes parameters are in black and blue, respectively. Red is the polarization P and green is the angle of polarization θ.

from Table 3.3. The best model we found was fixing Θ. The parameters found by the new D+D for σ Ori E are compatible with the results of Carciofi et al. (2013). The new D+D model improved the previous results, providing parameters with lower errors and a more precise characterization of σ Ori E's magnetosphere. Fig. 4.2 shows the star and geometry of the magnetosphere of the best parameters found by the D+D model, along with its corresponding (black dots in the graphs) Stokes parameters and polarization angle. The figures are snapshots of the star rotation at phases $\phi = 0$, 0.25, 0.50, and 0.75 (top left, top right, bottom left, and bottom right, respectively). The disk height and blobs sizes are proportional to the radius of the star.

The corner plot, which shows the probability density distribution of each parameter is shown in Fig. 4.4. It is possible to see that all parameters converge, and their density distributions are well defined. The errors were calculated within a 68% confidence interval of the posterior distribution.

In addition, the corner plot shows the correlations between each parameter; there are pairs of parameters strongly (anti-)correlated. In order to give this correlation we plot the correlation matrix in Fig. 4.3. The correlation matrix is calculated through the chains of the emcee algorithm, which contains the values of all the walkers for all parameters investigated by the model. For instance, there is a strong anti-correlation between Q_{IS} and U_{IS}. Such

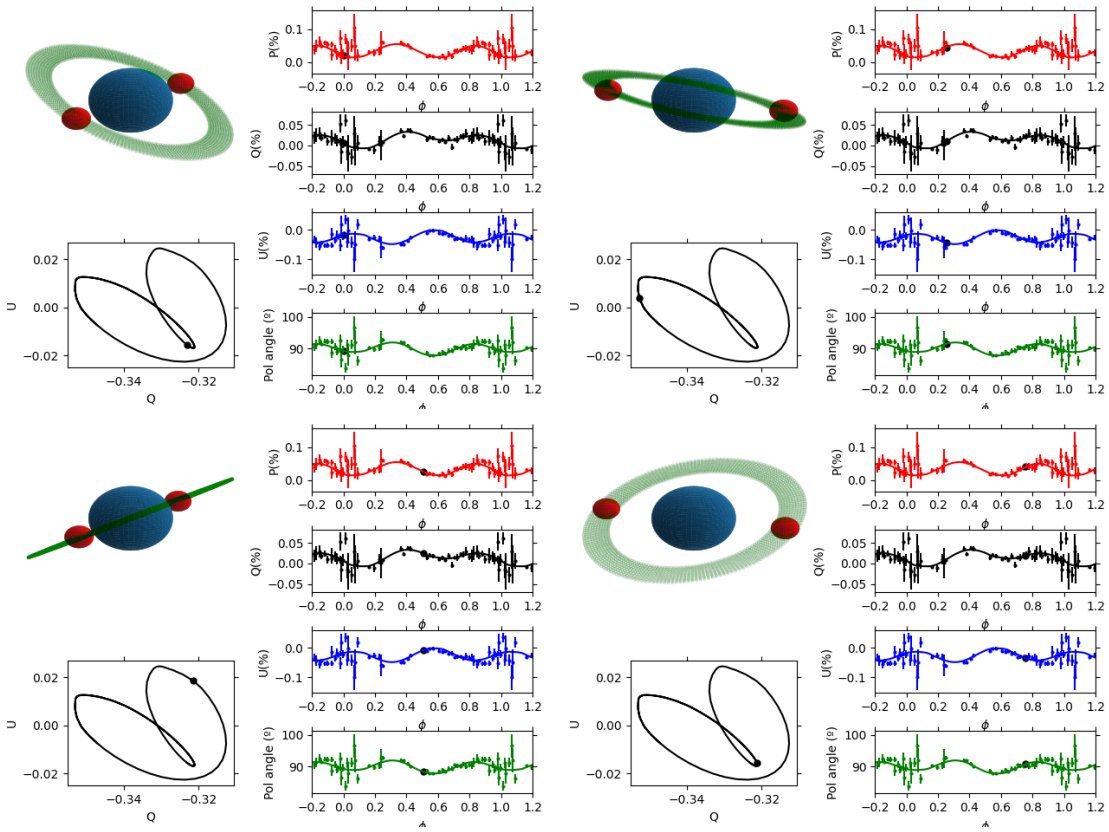

Figure 4.2: Snapshots of the magnetosphere of σ Ori E at rotational phases $\phi = 0$, 0.25, 0.50 and 0.75, along with the corresponding polarization at that phases (black dots). Bottom left of each panel is the QU diagram.

Table 4.2 - Comparison of the best parameters found by the new routine of the D+D model with the values found by the old method of analysis of Carciofi et al. (2013) for σ Ori E.

Parameters	New D+D	Old D+D
i (deg)	$77.5^{+1.9}_{-1.8}$	70 (Fixo)
n_e^b (e^-cm^{-3})	$1.25^{+0.15}_{-0.18} \times 10^{12}$	$1.0^{+0.6}_{-0.9} \times 10^{12}$
n_e^d (e^-cm^{-3})	$2.3^{+1.5}_{-0.7} \times 10^{12}$	$2.7 \pm 1.0 \times 10^{12}$
α (deg)	24^{+24}_{-12}	28
Q_{IS} (%)	$-0.350^{+0.008}_{-0.010}$	-0.35 ± 0.01
U_{IS} (%)	$0.028^{+0.015}_{-0.014}$	0.025 ± 0.010
Θ (deg)	150 (Fixed)	150 ± 7
δ	$0.086^{+0.03}_{-0.02}$	0.085 ± 0.02

high anti-correlation indicates that the parameters are degenerate – in this case, they could be represented by a single parameter, P. This happens because the angle of polarization does not change much during the rotation period of the star, compared to the intrinsic

polarization (see Figs. 2.4 and 2.6, and Eq. 2.9a). Thus, what really changes during the star rotation is the magnitude of the P vector, and not θ. There is also an anti-correlation between Q_{IS} and α. Due to the geometry of the magnetosphere, α is the main parameter that will control the Q_{IS} polarization. This shows that the interstellar polarization plays a major role in determining the geometry of the magnetosphere of σ Ori E.

Figs. 4.4 and 4.3 demonstrate the main advantage of using the MCMC technique: not only it reveals correlations that could otherwise be missed but provides a much better estimate of the associated uncertainties of each parameter.

The test done to the new D+D model with the observational data of σ Ori E was a success. The new statistical method to determine the parameters proved to be able to define the parameters of the magnetosphere of the star with higher precision, improving the results of Carciofi et al. (2013).

Figure 4.3: Correlation map of σ Ori E. The parameters, from left to right, are i, Q_{IS}, U_{IS}, α, n_e^b, n_e^d and δ.

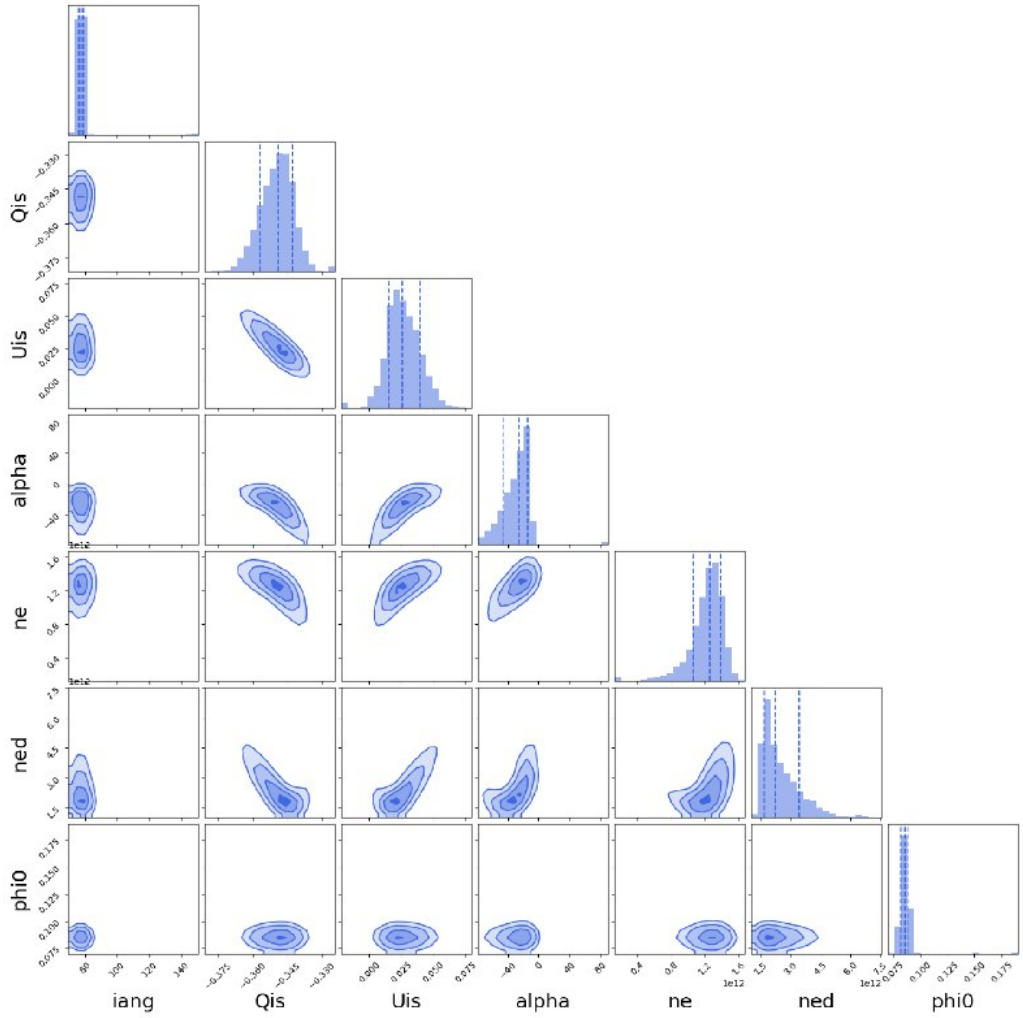

Figure 4.4: Corner plot of σ Ori E. The main diagonal shows the probability density distribution for each parameter, and the remaining squares the correlation between each pair.

4.3 HD 35502

4.3.1 Target Overview

HD 35502 is a He-weak star and the primary component of a triple system. The magnetic field of HD 35502 was first detected by Borra (1981) and later confirmed by Bychkov et al. (2005). It has an effective temperature of 18.4kK, a polar radius of $3.0R_{\odot}$ and mass of $5.7M_{\odot}$ (Sikora et al., 2016). Measurements of the Zeeman signatures in Stokes V parameter indicate a rotational period of 0.85 days and a magnetic field strength of 14kG (Sikora et al., 2016).

The variability of the strong H α emission (Fig 4.5) suggests two dense clouds magnetically confined that corotate with the star. The strength of the H α emission at phases 0.0 and 0.5 indicates two anti-symmetrical structures. The trajectory of the fitted dashed curves in Fig. 4.5 suggests that the clouds follow a nearly circular trajectory. Fig. 4.5 is a typical dynamical spectrum of stars of CMs.

4.3.2 Results

In our modeling of HD 35502, the values of the inclination $i = 24 \pm 10°$, the magnetic obliquity $\beta = 63 \pm 13°$ ($\alpha = 27 \pm 13°$) (Sikora et al., 2016) and the interstellar polarization (see Table 3.3 and Fig. B.1) were used as priors. The best fit found by our model and the intrinsic polarization of HD 35502 are in Fig. 4.6 and the parameters of the magnetosphere in Table 4.3. Fig. 4.7 shows the geometry of the magnetosphere and its corresponding polarization at phases $\phi = 0$, 0.25, 0.50, and 0.75. The corner plot of the model is shown in Fig. 4.8.

The D+D model fits very well the observational data, and HD 35502 has the second clearest modulation of our sample, the modulation amplitude, 0.015%, is three times the average observational error (0.005%). Although the value of $i = 46.7°$ is not compatible with the value used as a prior, the obliquity $\beta = 62°$ found is very close. One notable result is the difference in densities of the blobs and disk: the density of the disk is over ten times higher than the density of the blobs. This is probably due to the strength and geometry of the magnetic field.

The disk density of HD 35502 is about three times higher than the disk density of σ Ori E while the value of the obliquity is very similar for both stars. The phase lag δ is

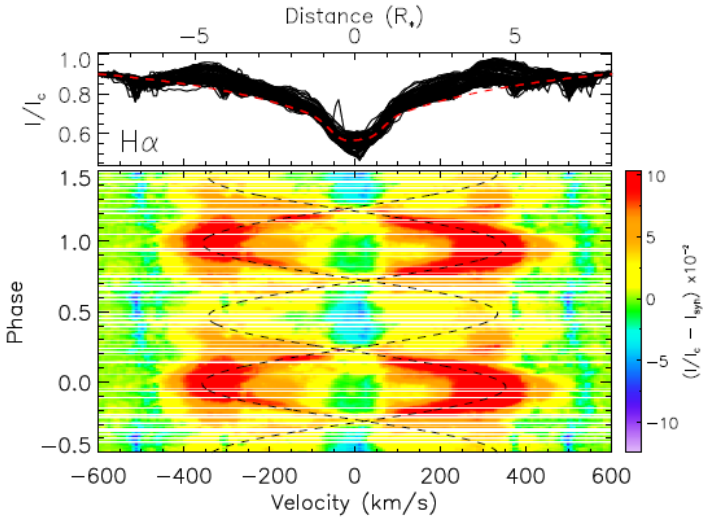

Figure 4.5: Top: Observed H α spectrum (I/I_c, black curve) of HD 35502 compared with the average synthetic spectrum (I_{syn}. Bottom: Dynamic spectra of $I/I_c - I_{syn}$. Image adapted from Sikora et al. (2016).

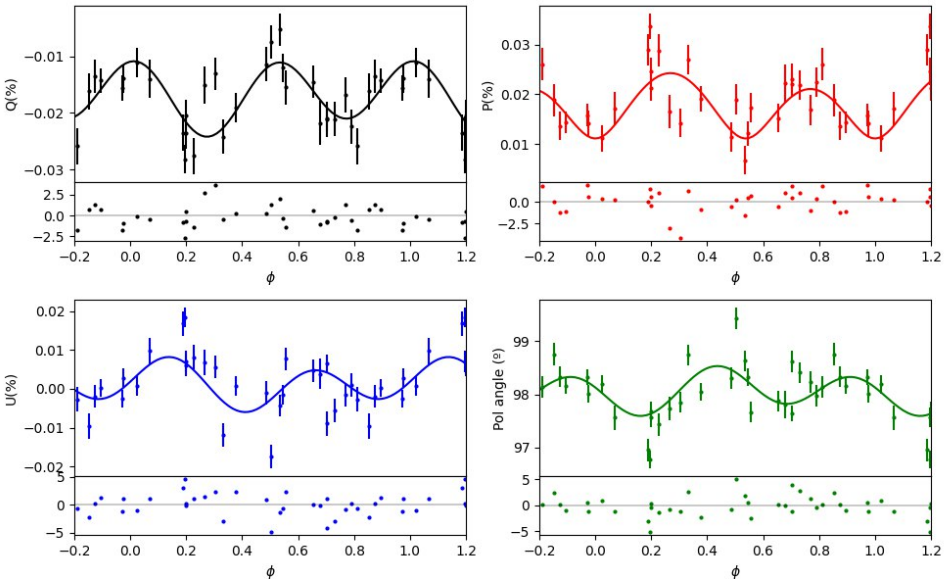

Figure 4.6: Same as Fig. 4.1 for HD 35502.

smaller in the case of HD 35502. In general, the parameters of HD 35502 have errors lower than σ Ori E's.

Fig. 4.9 shows the correlation map of the parameters found by the D+D model. The inclination angle i has a strong correlation to α and δ, and consequently, a correlation between α and δ is also seen. The correlation between i and α is due to the geometry of the line of sight and i and δ due to the asymmetry of the blobs.

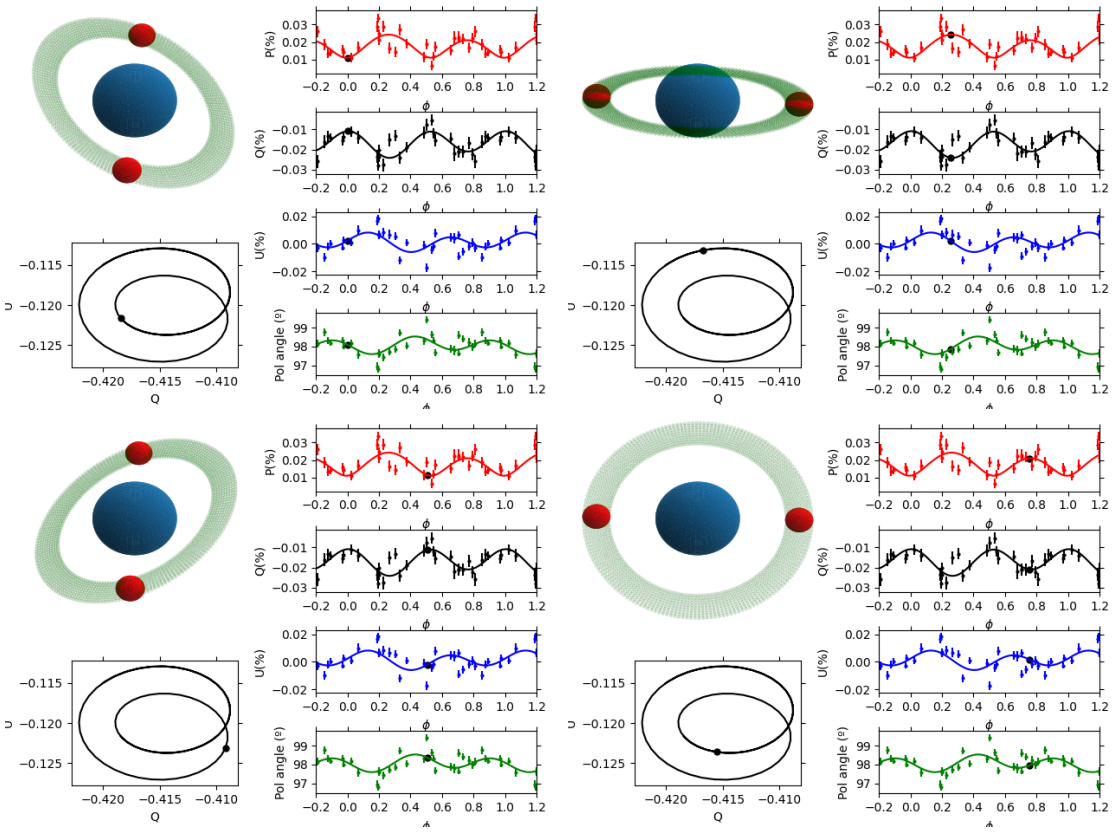

Figure 4.7: Same as Fig. 4.2 for HD 35502

Table 4.3 - Parameters of the best fit of HD 35502.

Parameters	Value
i (deg)	$48.0^{+0.8}_{-0.7}$
$n_e^b(e^-\mathrm{cm}^{-3})$	$2.04^{+0.76}_{-0.83} \times 10^{11}$
$n_e^d(e^-\mathrm{cm}^{-3})$	$5.12^{+1.12}_{-0.80} \times 10^{12}$
α (deg)	$28.2^{+3.6}_{-2.6}$
Q_{IS} (%)	$-0.397^{+0.003}_{-0.003}$
U_{IS} (%)	$-0.121^{+0.003}_{-0.005}$
Θ (deg)	$88.2^{+6.8}_{-5.0}$
δ	$0.021^{+0.027}_{-0.014}$

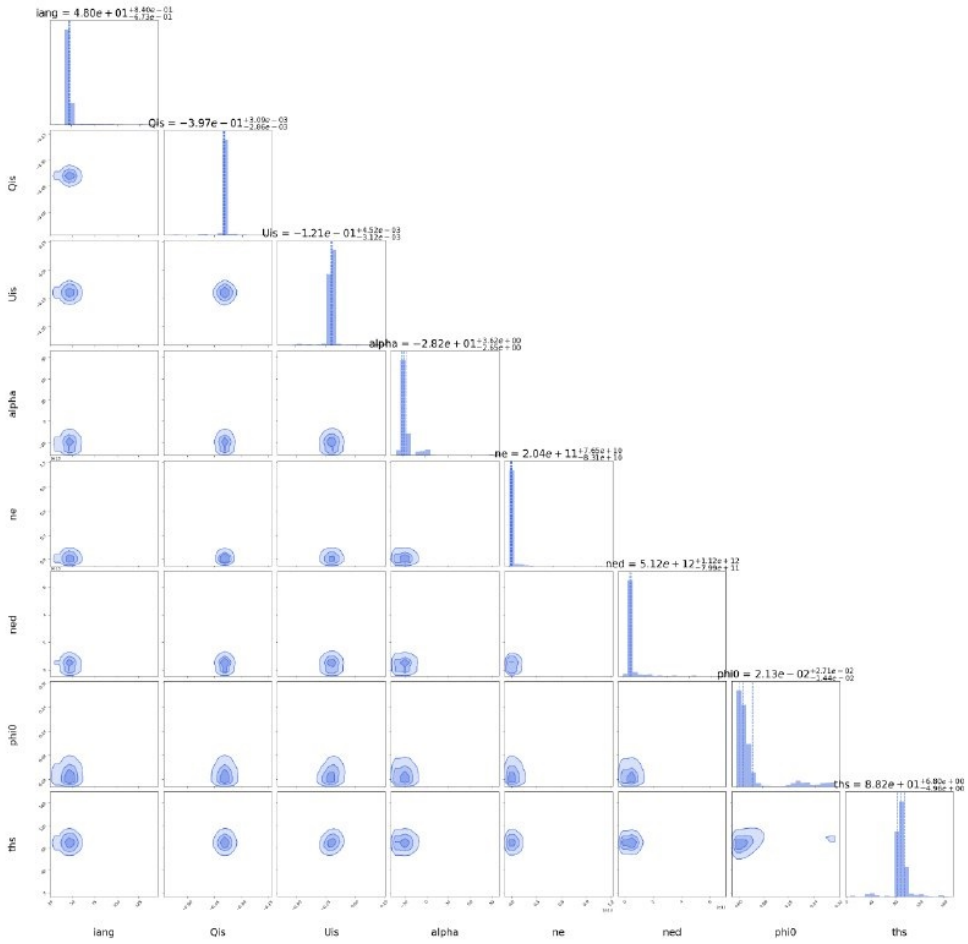

Figure 4.8: Corner plot of HD 35502.

Figure 4.9: Same as Fig. 4.3 for HD 35502.

4.4 HD 142990

4.4.1 Target Overview

Borra et al. (1983) were the first to detect the magnetic field of HD 142990. It has an effective temperature of 18kK, a radius of $2.8R_{\odot}$, mass of $5.7M_{\odot}$ and magnetic field strength of 4.3kG (Das et al., 2019). The star shows weak H α lines, especially on the blue wing (Fig. 4.10), and hints at the possible existence of a centrifugally driven wind originating a magnetosphere (Shore et al., 2004).

A recent determination of the rotation period of HD 142990 shows that the star suffers a spin-up of approximately -0.6s/yr (Shultz et al., 2018). One possible explanation of the spin-up may be the light-time effect, a distortion of the light in mid-eclipses time due to the orbit of a binary companion (Irwin, 1952). However, there is no evidence of a companion in the case of HD 142990 (Shatsky and Tokovinin, 2002). A second explanation may be that the star is still evolving towards the zero-age main sequence and that the spin-up is a consequence of the core-contraction (Shultz et al., 2018).

4.4.2 Results

We adopted a rotation period of $P = 0.979110$ days from Shultz et al. (2018), as it is the most used in literature. We used $i = 54.6 \pm 1.5°$ and $\beta = 89.84 \pm 3.01°$ ($\alpha = 0.16 \pm 3.01°$)

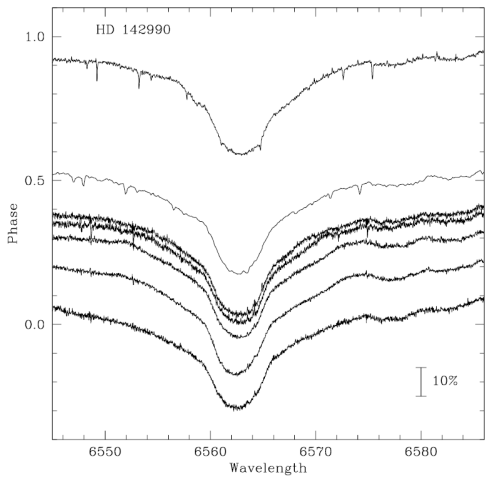

Figure 4.10: H α Observations of HD 142990. Each spectrum has been normalized to a continuum level of 1.0, the relative scale is shown on the bottom-right corner (Shore et al., 2004).

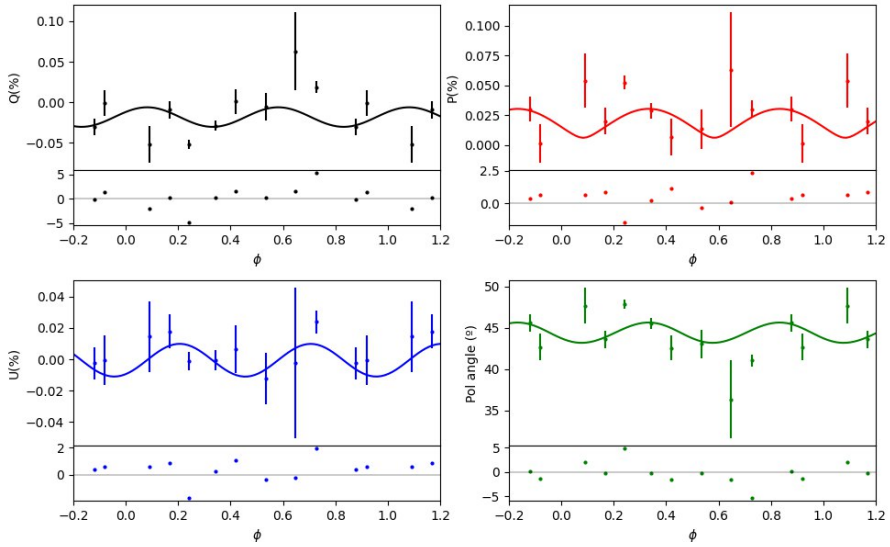

Figure 4.11: Same as Fig. 4.1 for HD 142990.

Table 4.4 - Parameters of the best fit of HD 142990.

Parameters	Value
i (deg)	$54.7^{+1.5}_{-1.5}$
n_e^b	$1.25^{+0.25}_{-0.25} \times 10^{11}$
n_e^d	$5.12^{+1.12}_{-0.80} \times 10^{12}$
α (deg)	$0.160^{+0.016}_{-0.016}$
Q_{IS} (%)	$0.017^{+0.007}_{-0.019}$
U_{IS} (%)	$0.287^{+0.008}_{-0.01}$
Θ (deg)	101^{+49}_{-19}
δ	$-0.10^{+0.14}_{-0.05}$

as priors in our code (Das et al., 2019). We limited the emcee algorithm to explore values for α between 0 and 90° since α cannot be lower than 0. We binned the phase of the data in intervals of 0.1 in order to increase the signal-to-noise ratio. We also applied a σ-clipping function of 2σ to remove outliers present in our data. The best fit and the intrinsic polarization of the star are shown in Fig. 4.11. The best parameters found by our model are in Table 4.4 and Fig. 4.12 shows the geometry of the magnetosphere and its corresponding polarization at phases $\phi = 0$, 0.25, 0.50 and 0.75.

There is a clear variation of the observed data several times above σ. The model, however, is only capable to capture a borderline modulation, especially for the Stokes

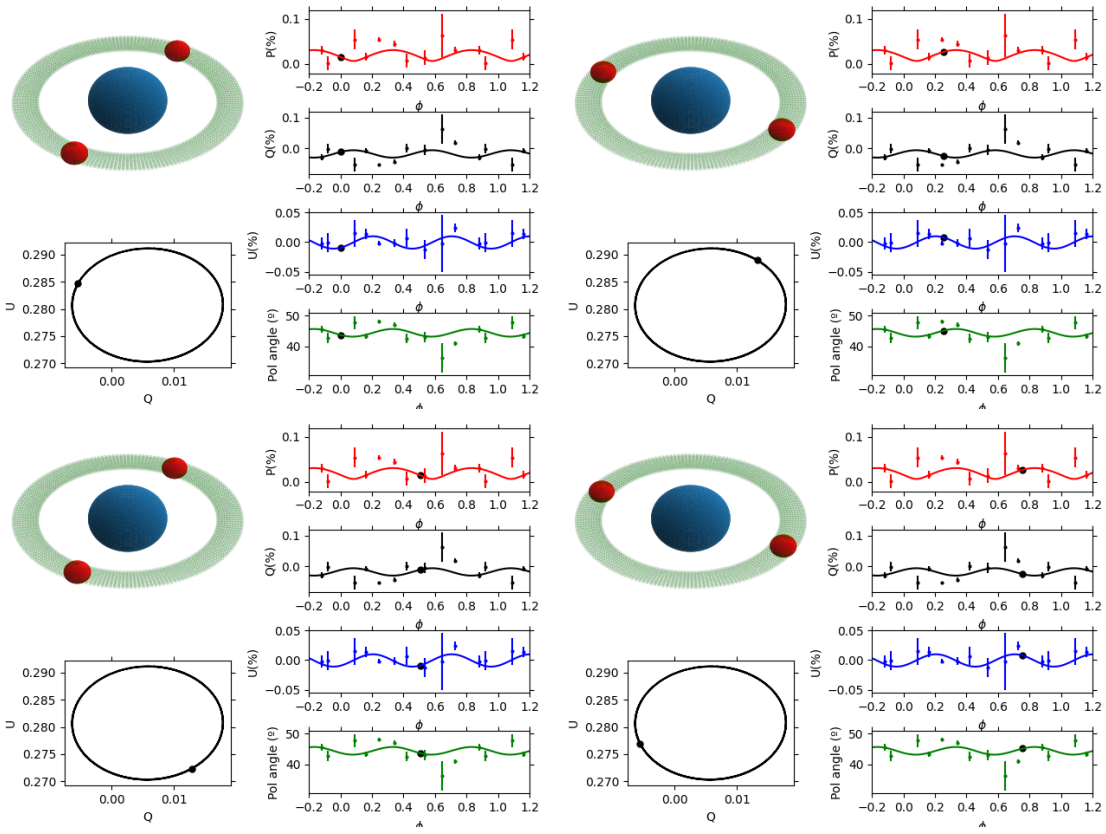

Figure 4.12: Same as Fig. 4.2 for HD 142990

parameter Q. This borderline modulation is reflected in the larger errors of the parameters, comparing the results to other models. This occurs specially for Q_{IS}, Θ, and δ, which have larger and strongly asymmetric errors. One possible explanation for this result is the geometry of the magnetic field. An obliquity of $\beta = 89.84°$ causes the effective potential to have two local minima, making the magnetosphere of HD 142990 to have a very peculiar shape (see Fig. 2.3). Since the linear polarization is very sensitive to the geometry of the circumstellar material, such a peculiar shape of the magnetosphere can no longer be represented by only a disk and a pair of blobs. Nonetheless, more observations of this star are necessary.

Fig. 4.13 shows the correlation map of the parameters of HD 142990 and Fig. 4.14 shows the corner plot. Most of the parameters do not have any correlation between each other, except the anti-correlation of δ and Θ to Q_{IS}, and of δ and Θ to U_{IS}. The strong anti-correlation between δ and Θ to $Q_{\rm IS}$ and $U_{\rm IS}$ can be explained by the fact that neither of them has a well-defined density distribution.

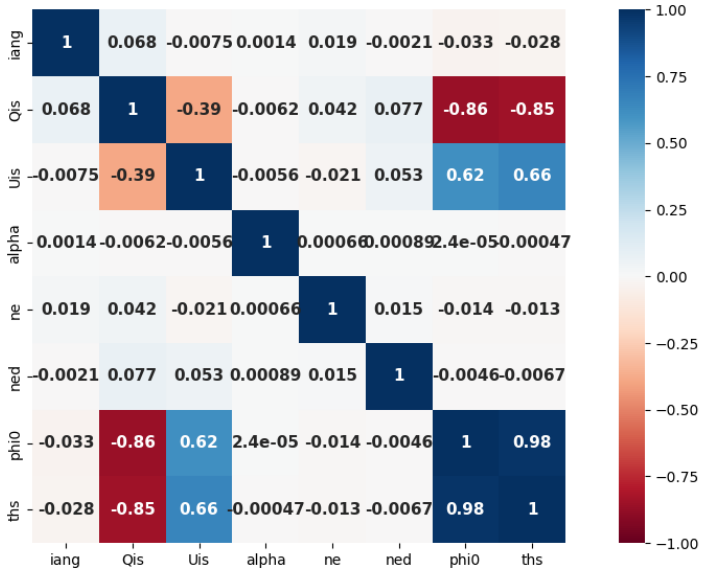

Figure 4.13: Same as Fig. 4.3 for HD 142990.

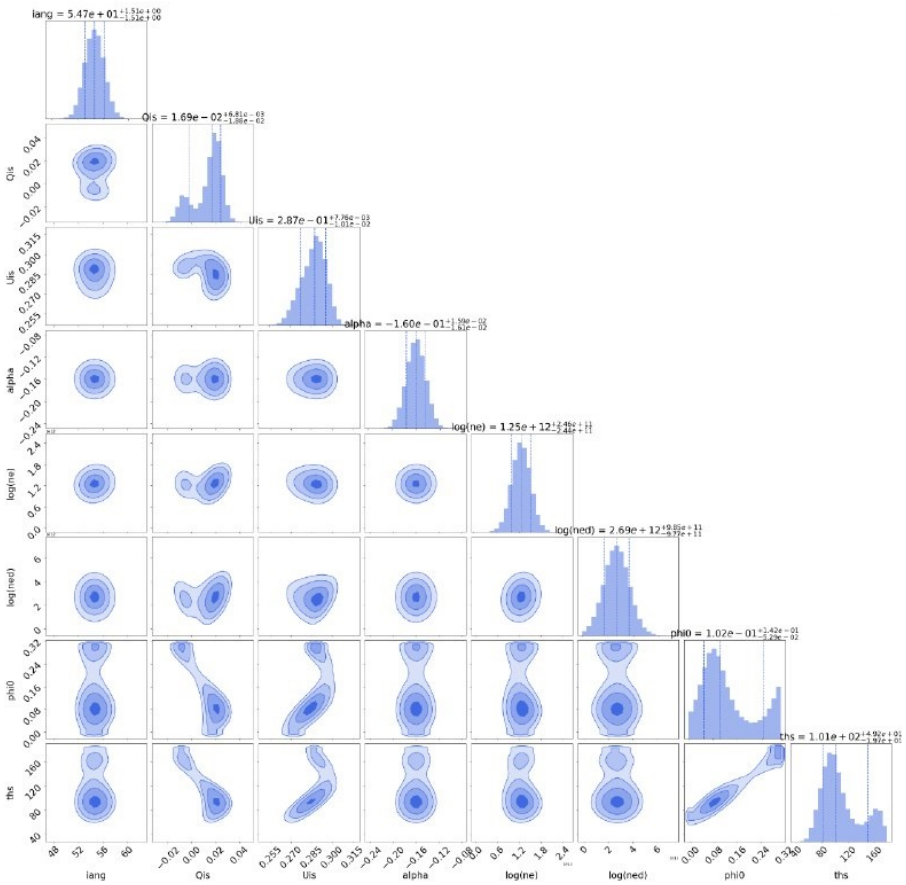

Figure 4.14: Corner plot of HD 142990.

4.5 HR 7355

4.5.1 Target Overview

HR 7355 (HD 182180) is a He-rich star with an effective temperature of 17.5kG, a mass of $6M_{\odot}$, radius of $3.69R_{\odot}$ and magnetic field strength of 11.6kG (Oksala et al., 2010). HR 7355 is one of the most luminous magnetic stars at radio wavelength, and observations of the longitudinal magnetic field and of radio and X-ray emissions, all oscillating in the same period, indicate that HR 7355 has a rotation period of 0.5214404 days (Leto et al., 2017). The dynamic spectrum of HR 7355 indicates the presence of a magnetosphere corotating with the star (Fig. 4.15).

4.5.2 Results

The priors used for modeling HR 7355 of $i = 60 \pm 10°$ and $\beta = 75 \pm 10°$ ($\alpha = 15 \pm 10°$) were taken from Leto et al. (2017). The interstellar polarization was measured by the field stars method (see Table 3.3 and Fig. B.2), $Q_{\rm IS} = -0.082(20)$, $U_{\rm IS} = -0.067(20)$, and were used as a prior to the model as well. In order to improve the quality of the data, we binned the data in phase intervals of 0.1 and applied a σ-clip function of 2σ.

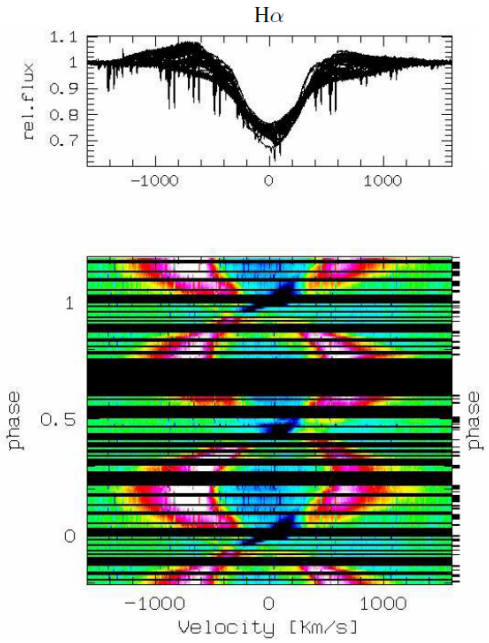

Figure 4.15: Dynamical spectrum of HR 7355, indicating the existence of a magnetosphere with two roughly anti-symmetrical blobs. Top: overplotted H α profiles. Bottom: phase variations (Rivinius et al., 2013).

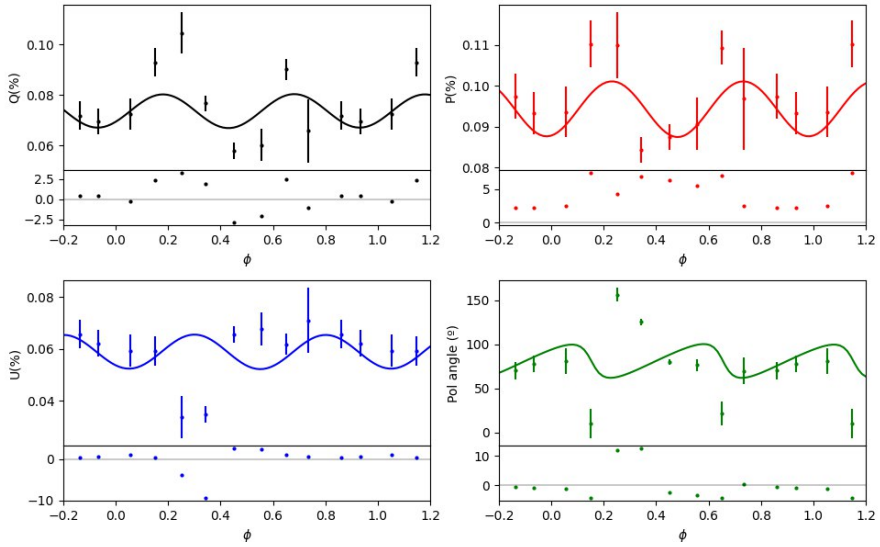

Figure 4.16: Same as Fig. 4.1 for HR 7355.

Table 4.5 - Parameters of the best fit of HR 7355.

Parameters	Value
i (deg)	$45.5^{+0.7}_{-0.6}$
n_e^b	$7.7^{+1.2}_{-1.2} \times 10^{11}$
n_e^d	$2.16^{+0.20}_{-0.19} \times 10^{13}$
α (deg)	$14.8^{+1.7}_{-1.6}$
Q_{IS} (%)	$-0.080^{+0.009}_{-0.009}$
U_{IS} (%)	$-0.058^{+0.007}_{-0.006}$
Θ (deg)	$19.9^{+2.4}_{-2.1}$
δ	$0.036^{+0.17}_{-0.014}$

Fig. 4.16 shows the intrinsic polarization of the star and the best fit found by the D+D model. The parameters of the magnetosphere are in Table 4.5. Fig. 4.17 shows the geometry of the magnetosphere and its corresponding polarization at phases $\phi = 0$, 0.25, 0.50, and 0.75.

There is a clear variation of the intrinsic polarization of HR 7355, but the model could not reproduce the details of the variation. The model has practically found the same value for the obliquity ($\alpha = 14.8°$) of Leto et al. (2017). The interstellar polarization of the model is compatible with the values measured using the method of field stars. In fact, the model cannot find any reasonable result if we do not use the interstellar polarization

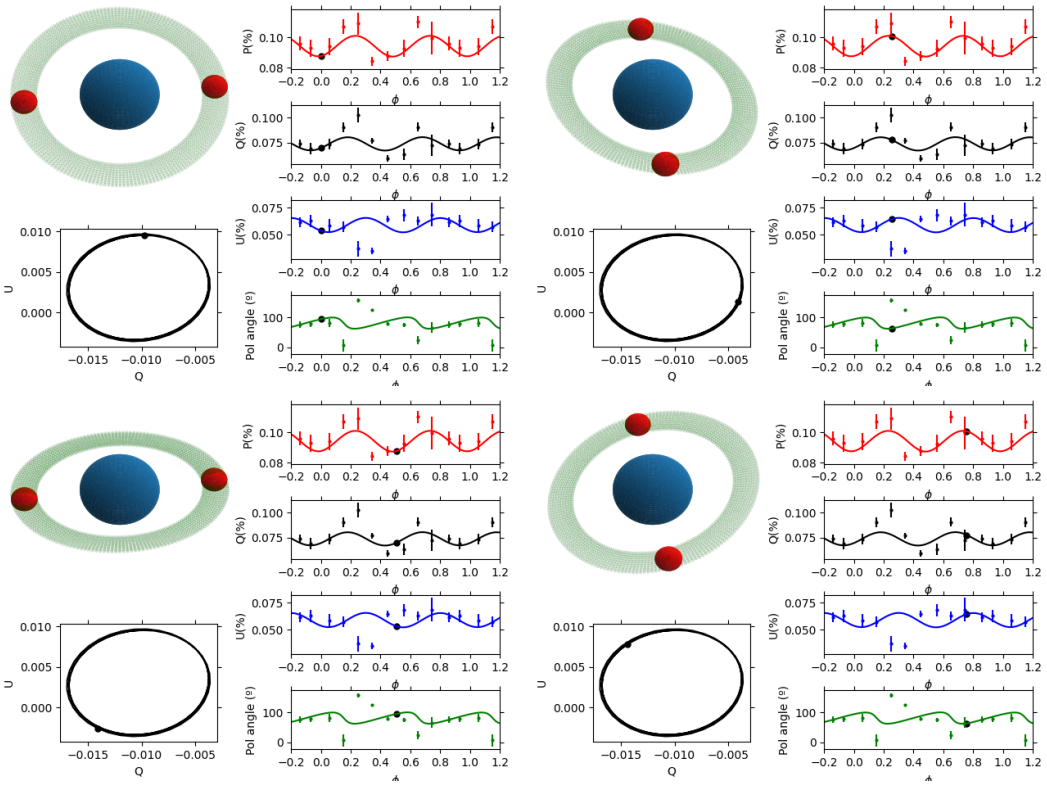

Figure 4.17: Same as Fig. 4.2 for HR 7355.

as priors, since the observed polarization is small and close to the detection limit of the polarimeter. The density of the disk is much higher than the density of the blobs, which contradicts the dynamical spectrum of Rivinius et al. (2013). New tests with a model of only blobs or only disk are necessary in order to improve the results.

The polarization angle (bottom right in Fig. 4.16) shows an acute disagreement between the observational data and the model between phases 0.1 and 0.4, this is a strong indication that the model does not reproduce the geometry of the magnetosphere correctly and need to be further improved. We plan to carry out new observations of HR 7355 at OPD in order to improve the S/N.

Fig. 4.18 shows to correlation map of HR 7355, and the corner plot is shown in Fig. 4.19. There is an anti-correlation of Q_{IS} and α, due to the geometry of the magnetosphere. There is also a correlation of i and Θ, the inclination angle determines the rotational axis of the line of sight.

Figure 4.18: Same as Fig. 4.3 for HR 7355.

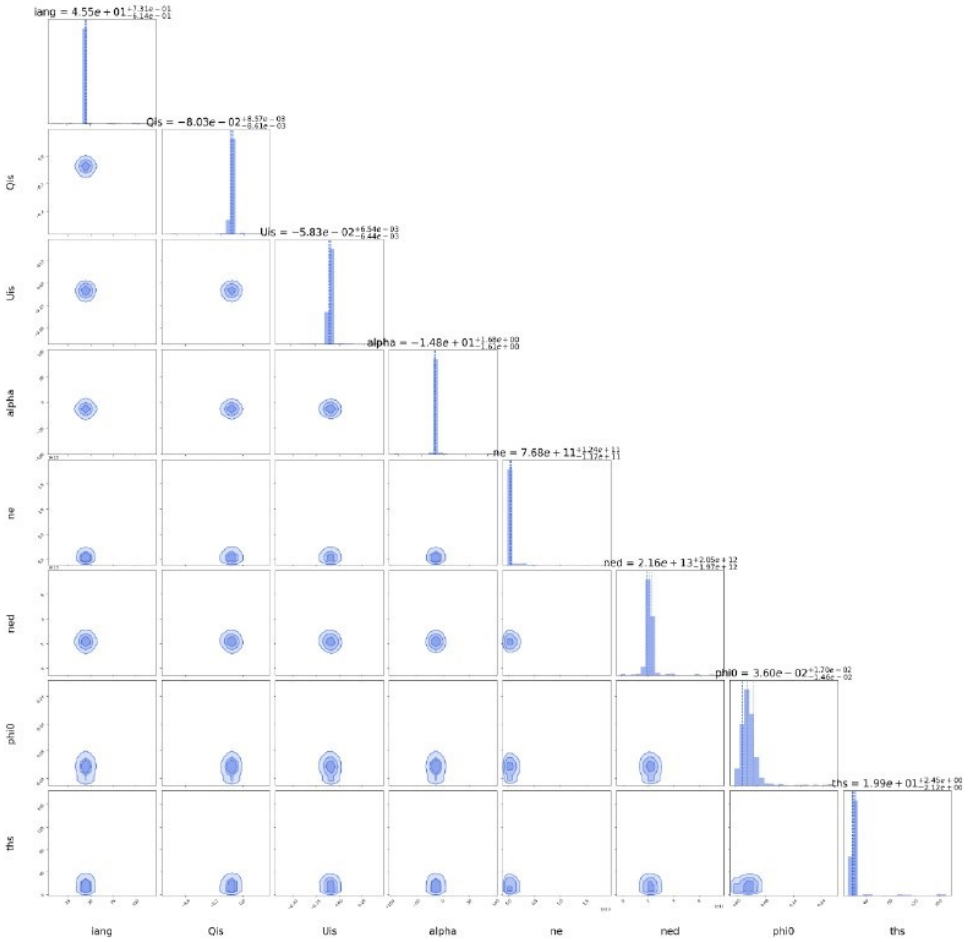

Figure 4.19: Corner plot of HR 7355.

4.6 HR 5907

4.6.1 Target Overview

HR 5907 (HD 142184) is a He-strong main sequence star with a mass of $5.5M_{\odot}$, radius of $3.1R_{\odot}$ and a temperature of 17kK (Grunhut et al., 2012). HR 5907 presents evidence of photometric and spectroscopic variability with a period of 0.508276 days (Fig. 4.20). Among all the currently known non-degenerated magnetic OB stars, HR 5907 has the shortest rotation period. Measurements of the longitudinal magnetic field phase coherently with the rotation period imply a surface dipole field strength of approximately 15.7kG (Grunhut et al., 2012). On the other hand, Bayesian analysis using the Least-Squares Deconvolution technique of the Stokes V profile indicates a dipolar field strength of approximately 10.4kG (Grunhut et al., 2011). This disagreement suggests a surface magnetic field configuration more complex with contributions from higher-order multipolar components or from the non-uniform Helium surface abundance distribution.

Radio/millimeter observations made with the VLA and ALMA interferometers found that HR 5907 is the most radio luminous early type star in the centimeter-millimeter band known to date (Leto et al., 2018). The radio emission can be explained by the non-thermal electrons present in the current sheets that are being accelerated on the outer border of the magnetosphere. In addition, simulations of the radio emission of HR 5907 also indicate that the star is likely to have a more complex magnetic field topology than a simple dipole (Leto et al., 2018).

Unlike the others magnetic stars, there is no anti-symmetry in the dynamic spectrum of HR 5907 (Fig. 4.20). This is probably due to the non-dipolar magnetic field, which would cause a non-symmetric magnetosphere.

4.6.2 Results

The inclination $i = 70 \pm 10^{\circ}$ and $\beta = 7^{+2}_{-1}{}^{\circ}$ ($\alpha = 83^{\circ}$) taken from Grunhut et al. (2011) were used as priors in our code, along with the interstellar polarization (Table 3.3 and Fig. B.3). The observed data and the best fit of the D+D model are shown in Fig. 4.21. The best parameters found are in Table 4.6. We applied a σ-clip function of 2σ to remove outliers from our data and binned the data in phase intervals of 0.1. Fig. 4.22 shows the geometry of the magnetosphere and its corresponding polarization at phases $\phi = 0$, 0.25,

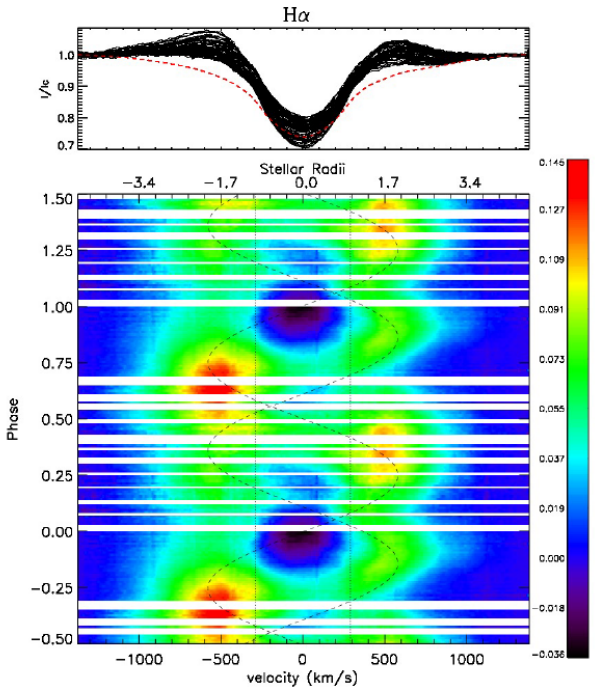

Figure 4.20: Phased observational variations of the Hα line of HR 5907 magnetosphere. Green to red highlights emission and blue to black indicates absorption. Image adapted from Grunhut et al. (2011).

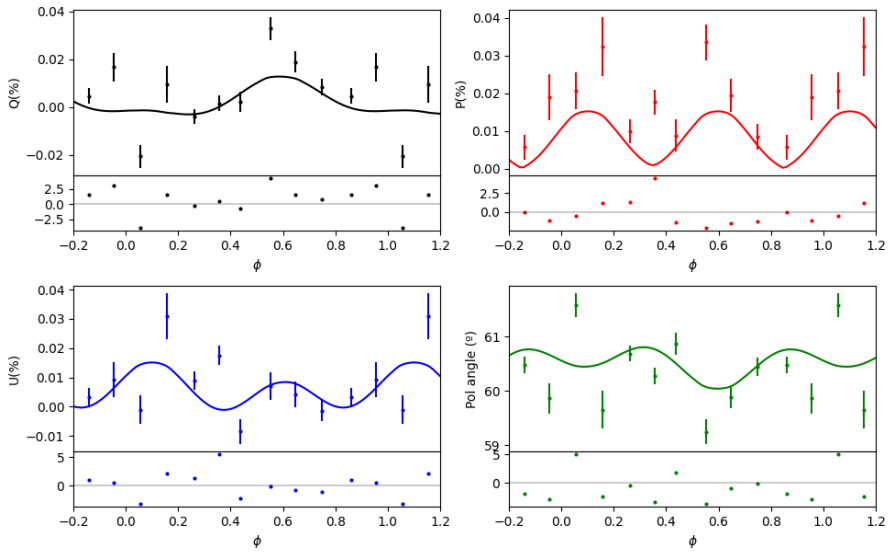

Figure 4.21: Same as Fig. 4.1 for HR 5907

0.50, and 0.75.

It is possible the see a small modulation in the data. However, this modulation is minimal (lower than 0.05%). The density of the blobs is the lowest of all models, while the disk density is similar. The fact that the blobs have such low density and that it is

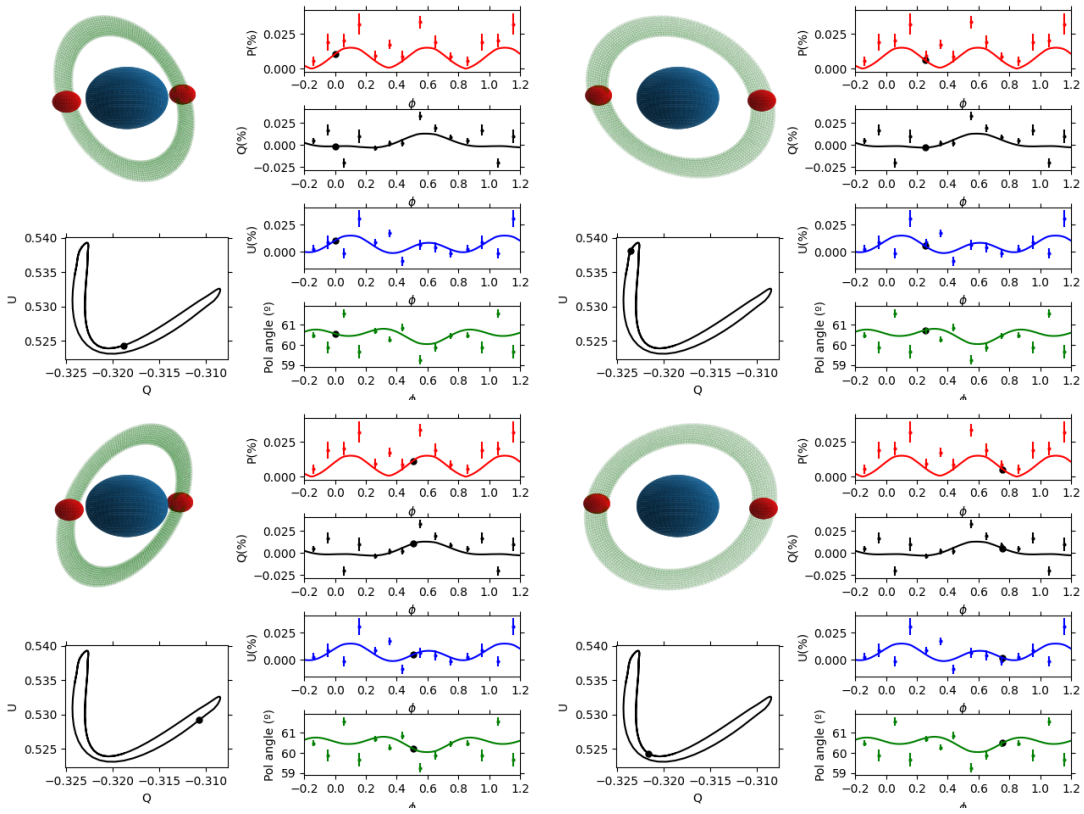

Figure 4.22: Same as Fig. 4.2 for HR 5907

Table 4.6 - Parameters of the best fit of HR 5907.

Parameters	Value
i (deg)	$87.7^{+4.1}_{-4.5}$
n_e^b (e^-cm^{-3})	$5^{+10}_{-1} \times 10^8$
n_e^d (e^-cm^{-3})	$2.18^{+0.28}_{-0.41} \times 10^{12}$
α (deg)	$75.7^{+0.5}_{-1.1}$
Q_{IS} (%)	$-0.322^{+0.002}_{-0.002}$
U_{IS} (%)	$-0.525^{+0.002}_{-0.002}$
Θ (deg)	120^{+4}_{-5}
δ	$0.094^{+0.004}_{-0.009}$

not very well defined (see Fig. 4.23) is a strong indication that the results of the modeling of HR 5907 are not reliable. The inclination angle i is higher than the value used as prior, and the obliquity α is somewhat close. The interstellar polarization is very close to the values used as priors and has the smallest errors of all models.

The fact that HR 5907 probably has a magnetic field topology more complex than a

simple dipole can explain the failure of modeling with the D+D. The RRM model was created assuming a dipole magnetic field, where the material would settle where the potential undergoes a local minimum. A magnetic field with a different topology would cause this potential to be completely different, and the star's magnetosphere would have a completely distinct shape. In this case, a simple model with a disk and two blobs might fail completely to capture the essence of the magnetosphere's spatial configuration. New tests adopting a model with disk or blobs only might reproduce the observational data more precisely.

Basically all the parameters of HR 5907 have a strong correlation with each other (Fig. 4.24). A result where all the parameters are dependent on each other is another indication that the D+D failed to characterize the magnetosphere of HR 5907.

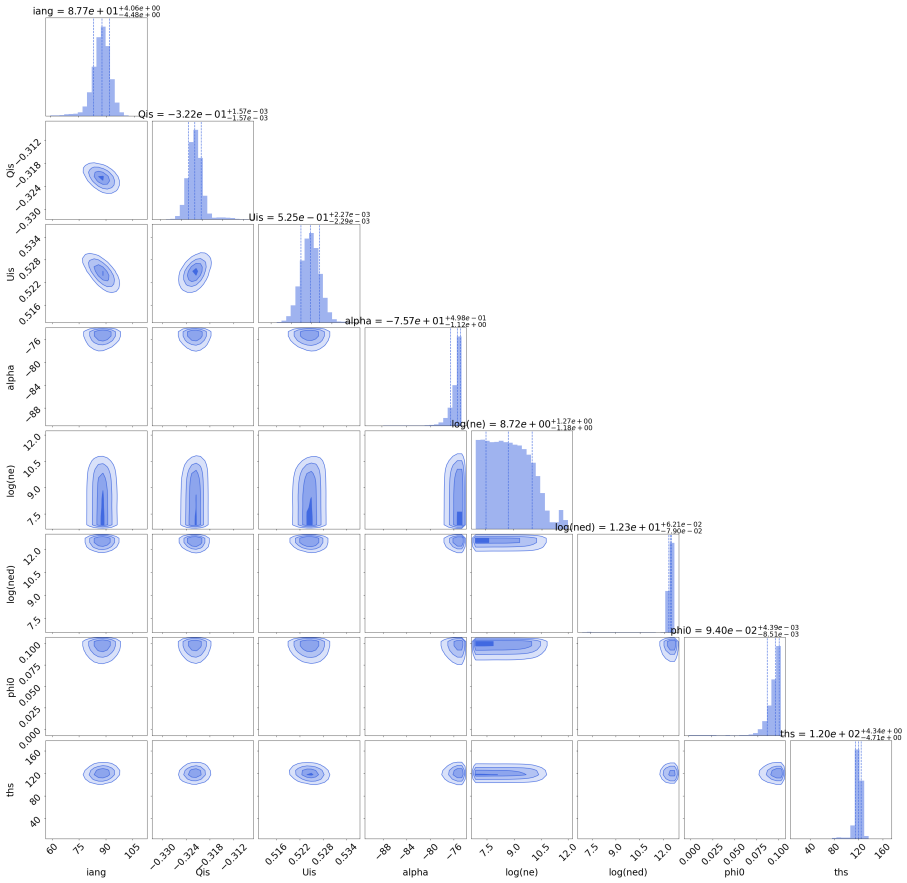

Figure 4.23: Corner plot of HR 5907.

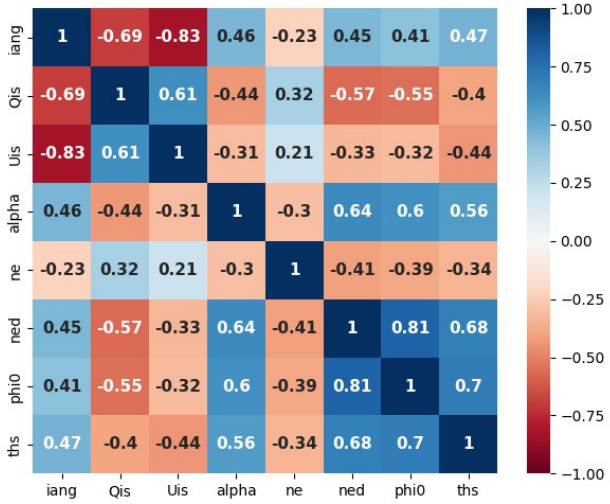

Figure 4.24: Same as Fig. 4.3 for HR 5907.

Chapter 5

Analysis and Discussion

The process of detection of massive stars' magnetospheres through their linear polarization is rather challenging. The observed polarization is very small, of the order of 0.01%, and the variation of polarization over the period of rotation of the star can be even smaller. The determination of the interstellar polarization by the star field method has proven to be an important prior for better modeling by the D+D. Since in the frame of the D+D model what controls the polarization of each of its components is the total mass of scatters (see Sec. 2.3.2). The distinction between interstellar and intrinsic polarization is fundamental to determining the density of the magnetosphere. Table 5.1 shows the average intrinsic polarization of the magnetospheres and their total masses. The polarization is of the order 0.05%, except for HR 7355, which has an intrinsic polarization of 0.1%. Interestingly, HR 7355 was the star with the lowest polarization observed. Fig. 5.1 shows the intrinsic polarization as a function of the total mass of magnetospheres. It was found a clear relation that more massive magnetospheres have a higher intrinsic polarization.

Table 5.1 - Average intrinsic polarization of the stars modeled by the D+D model and the total mass of their magnetospheres.

	$\langle P_{\rm int} \rangle$	Total Mass (Moon Mass)
σ Ori E	0.041 ± 0.018	5.6×10^{-4}
HD35502	0.048 ± 0.007	1×10^{-3}
HR5907	0.043 ± 0.026	2.2×10^{-4}
HR7355	0.103 ± 0.027	1.6×10^{-3}
HD142990	0.029 ± 0.019	2×10^{-4}

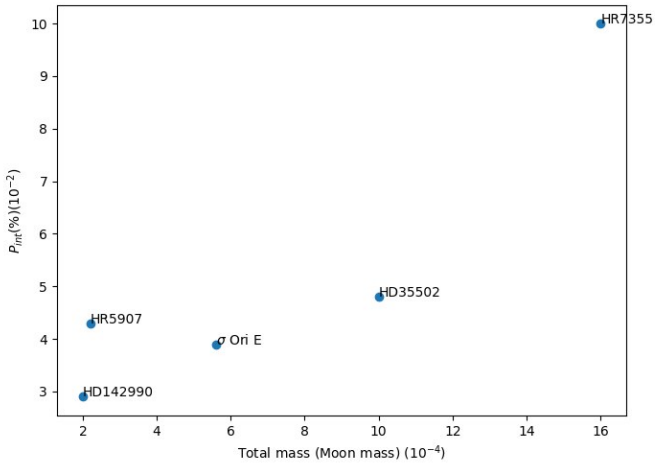

Figure 5.1: Intrinsic polarization of the magnetospheres modeled by the D+D model as a function of their masses (lunar masses).

Another interesting aspect to study is how the total mass of the magnetosphere relates to the strength of the magnetic field of its host star. According to Eq. 1.1, a star with a stronger magnetic field should have a higher η_*, and therefore should trap more material, increasing the total mass of the magnetosphere. Fig. 5.2 shows the total mass of the magnetosphere as a function of the strength of the magnetic field of its host star. If we exclude HR 7355 and HR 5907, the two stars for which the D+D model failed, there is a clear correlation between the magnetosphere mass and magnetic field strength.

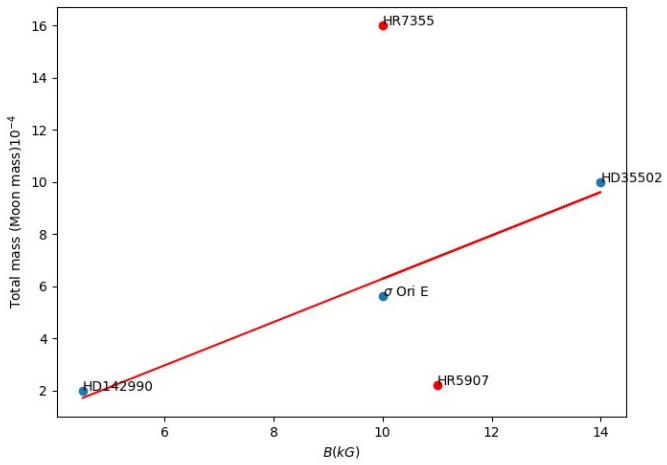

Figure 5.2: Total mass of the magnetosphere (moon mass) as a function of the strength of the magnetic field of its host star.

Chapter 6

Conclusions and Perspectives

In this work, we performed a study of OB stars with strong magnetic fields and short rotation periods, that are capable of sustaining a magnetosphere. In particular, we studied the circumstellar material of these stars through their linear polarization. After carrying out a series of observations at Observatório Pico dos Dias (OPD), we have data for 18 magnetic OB stars. We have completed the phase coverage for five of them, which we investigated further with the D+D model. Six of the stars have more than 50% of their rotational phases observed, and we plan to complete their observations in the near future.

We improved the statistical analysis of the Dumbbell plus Disk (D+D) model by coupling the routine to emcee, a Monte Carlo Markov Chain algorithm. The new D+D was capable to model the magnetosphere of σ Ori E, improving the results of Carciofi et al. (2013). We also applied the D+D to four new stars, HD 35502, HD 142990, HR 7355, and HR 5907, and reported new polarimetric detection of their magnetospheres through linear polarization.

The D+D fitted the observational data of HD 35502 very well, and made it possible to estimate the mass of the components of the magnetosphere. After σ Ori E, it is the second best modeling done by the D+D model. In the case of HD 142990, a polarization modulation was clearly detected in the data; however, the D+D was not capable of reproducing all aspects of the observations. This is probably because of the geometry of the magnetic field, with such a high obliquity ($\beta = 89.86°$), the magnetosphere cannot be fully represented by the model. For HR 7355, thanks to the precise estimates of the interstellar polarization, we could also detect the magnetosphere polarization, which has only a rather weak modulation. The D+D model failed to capture the details of the observations for this star. A similar situation was found for HR 5907. We present a firm detection of the

magnetosphere in polarization, with a small (but statistically significant) modulation. The D+D model was not successful for this star, which has the added complication of having a magnetic field more complex than a simple dipole.

Magnetospheres have a mass of about $10^{-3}M_{moon}$. We also study the relation of the mass of the magnetosphere with the strength of the magnetic field of its host star. As expected, there is a clear correlation between the mass and strength of the field.

The next steps are to continue the monitoring of magnetic stars at OPD. We will give priority to stars with near-complete phase coverage and apply their data to the D+D model.

Bibliography

Bjorkman J., Bjorkman K., The effects of gravity darkening on the ultraviolet continuum polarization produced by circumstellar disks, The Astrophysical Journal, 1994, vol. 436, p. 818

Borra E., Decaying stellar magnetic fields, magnetic braking-Evidence from magnetic observations in Orion OB1, The Astrophysical Journal, 1981, vol. 249, p. L39

Borra E., Landstreet J., The magnetic fields of the AP stars, The Astrophysical Journal Supplement Series, 1980, vol. 42, p. 421

Borra E., Landstreet J., Thompson I., The magnetic fields of the helium-weak B stars, The Astrophysical Journal Supplement Series, 1983, vol. 53, p. 151

Borra E. F., Landstreet J., The magnetic field of the helium-strong stars, The Astrophysical Journal, 1979, vol. 228, p. 809

Braithwaite J., Spruit H. C., A fossil origin for the magnetic field in A stars and white dwarfs, nature, 2004, vol. 431, p. 819

Bychkov V., Bychkova L., Madej J., A catalog of stellar magnetic rotational phase curves, Astronomy & Astrophysics, 2005, vol. 430, p. 1143

Carciofi A., Okazaki A., Le Bouquin J.-B., Štefl S., Rivinius T., Baade D., Bjorkman J., Hummel C., Cyclic variability of the circumstellar disk of the Be star ζ Tauri-II. Testing the 2D global disk oscillation model, Astronomy & Astrophysics, 2009, vol. 504, p. 915

Carciofi A. C., Faes D. M., Townsend R. H., Bjorkman J. E., Polarimetric Observations of σ Orionis E, The Astrophysical Journal, 2013, vol. 766, p. L9

Carciofi A. C., Magalhães A. M., Transporte radioativo em envoltórios circunstelares usando o método de Monte Carlo. PhD Thesis – Universidade de São Paulo, São Paulo, 2001.

Castor J. I., Abbott D. C., Klein R. I., Radiation-driven winds in Of stars, The Astrophysical Journal, 1975, vol. 195, p. 157

Das B., Chandra P., Shultz M. E., Wade G. A., Detection of coherent emission from the Bp star HD 142990 at uGMRT frequencies, The Astrophysical Journal, 2019, vol. 877, p. 123

Donati J.-F., Babel J., Harries T., Howarth I., Petit P., Semel M., The magnetic field and wind confinement of θ 1 Orionis C, Monthly Notices of the Royal Astronomical Society, 2002, vol. 333, p. 55

Donati J.-F., Howarth I., Jardine M., Petit P., Catala C., Landstreet J., Bouret J., Alecian E., Barnes J., Forveille T., et al., The surprising magnetic topology of τ Sco: fossil remnant or dynamo output?, Monthly Notices of the Royal Astronomical Society, 2006, vol. 370, p. 629

Faes D. M., An interferometric view of hot star disks, arXiv preprint arXiv:1512.06094, 2015

Foreman-Mackey D., Hogg D. W., Lang D., Goodman J., emcee: the MCMC hammer, Publications of the Astronomical Society of the Pacific, 2013, vol. 125, p. 306

Groote D., Hunger K., Shell and photosphere of Sigma ORI E-New observations and improved model, Astronomy and Astrophysics, 1982, vol. 116, p. 64

Grunhut J., Rivinius T., Wade G., Townsend R., Marcolino W., Bohlender D., Szeifert T., Petit V., Matthews J., Rowe J., et al., HR 5907: Discovery of the most rapidly rotating magnetic B-type star by the MiMeS Collaboration, arXiv preprint arXiv:1109.3157, 2011

Grunhut J., Rivinius T., Wade G., Townsend R., Marcolino W., Bohlender D., Szeifert T., Petit V., Matthews J., Rowe J., et al., HR 5907: Discovery of the most rapidly rotating magnetic early B-type star by the MiMeS Collaboration, Monthly Notices of the Royal Astronomical Society, 2012, vol. 419, p. 1610

Grunhut J., Wade G., Sundqvist J., Ud-Doula A., Neiner C., Ignace R., Marcolino W., Rivinius T., Fullerton A., Kaper L., et al., Investigating the spectroscopic, magnetic and circumstellar variability of the O9 subgiant star HD 57682, Monthly Notices of the Royal Astronomical Society, 2012, vol. 426, p. 2208

Hall J. S., Observations of the polarized light from stars, Science, 1949, vol. 109, p. 166

Hamaker J., Bregman J., Sault R., Understanding radio polarimetry. I. Mathematical foundations, Astronomy and Astrophysics Supplement Series, 1996, vol. 117, p. 137

Henrichs H., Kolenberg K., Plaggenborg B., Marsden S., Waite I., Landstreet J., Wade G., Grunhut J., Oksala M., Discovery of a magnetic field in the early B-type star σ Lupi, Astronomy & Astrophysics, 2012, vol. 545, p. A119

Hesser J. E., Walborn N. R., Patricio U. P., Sigma Orionis E as a mass-transfer binary system, Nature, 1976, vol. 262, p. 116

Hiltner W., Polarization of light from distant stars by interstellar medium, Science, 1949, vol. 109, p. 165

Hubrig S., Kholtygin A., Schöller M., Ilyin I., Characterizing the magnetic field and spectral variability of the rigidly rotating magnetosphere star HD 345439, Monthly Notices of the Royal Astronomical Society: Letters, 2017, vol. 467, p. L81

Irwin J. B., The determination of a light-time orbit., The Astrophysical Journal, 1952, vol. 116, p. 211

Klement R., Carciofi A., Rivinius T., Panoglou D., Vieira R., Bjorkman J., Štefl S., Tycner C., Faes D., Korčáková D., et al., Multitechnique testing of the viscous decretion disk model-I. The stable and tenuous disk of the late-type Be star β CMi, Astronomy & Astrophysics, 2015, vol. 584, p. A85

Krtička J., Janík J., Marková H., Mikulášek Z., Zverko J., Prvák M., Skarka M., Ultraviolet and visual flux and line variations of one of the least variable Bp stars HD 64740, Astronomy & Astrophysics, 2013, vol. 556, p. A18

Landstreet J., Borra E. F., The magnetic field of Sigma Orionis E, The Astrophysical Journal, 1978, vol. 224, p. L5

Lazarian A., Magnetic fields via polarimetry: progress on grain alignment theory, Journal of Quantitative Spectroscopy and Radiative Transfer, 2003, vol. 79, p. 881

Leone F., Bohlender D., Bolton C., Buemi C., Catanzaro G., Hill G., Stift M., The magnetic field and circumstellar environment of the helium-strong star HD 36485= δ Ori C, Monthly Notices of the Royal Astronomical Society, 2010, vol. 401, p. 2739

Leone F., Umana G., Periodic radio emission from the helium strong stars HD 37017 and Sigma ORI E, Astronomy and Astrophysics, 1993, vol. 268, p. 667

Leto P., Trigilio C., Oskinova L., Ignace R., Buemi C. S., Umana G., Ingallinera A., Todt H., Leone F., The detection of variable radio emission from the fast rotating magnetic hot B-star HR 7355 and evidence for its X-ray aurorae, Monthly Notices of the Royal Astronomical Society, 2017, vol. 467, p. 2820

Leto P., Trigilio C., Oskinova L. M., Ignace R., Buemi C. S., Umana G., Ingallinera A., Leone F., Phillips N., Agliozzo C., et al., A combined multiwavelength VLA/ALMA/Chandra study unveils the complex magnetosphere of the B-type star HR5907, Monthly Notices of the Royal Astronomical Society, 2018, vol. 476, p. 562

Livio M., Villaver E., Massive Stars: From Pop III and GRBs to the Milky Way. No. 20, Cambridge University Press, 2009

Maeder A., Evolution and nucleosynthesis in massive stars with mass loss-The yields in helium and heavy elements and constraints on the past star formation rate, Astronomy and Astrophysics, 1981, vol. 101, p. 385

Maeder A., Conti P. S., Massive star populations in nearby galaxies, Annual Review of Astronomy and Astrophysics, 1994, vol. 32, p. 227

Magalhaes A., Circumstellar Matter Studied with Polarimetry, Circumstellar Dynamics at High Resolution, 2012, vol. 464, p. 25

Magalhães A., Rodrigues C., Margoniner V., Pereyra A., Heathcote S., High precision CCD imaging polarimetry. In Polarimetry of the interstellar medium , vol. 97, 1996, p. 118

Maier D., Tenzer C., Santangelo A., Point and interval estimation on the degree and the angle of polarization: a Bayesian approach, Publications of the Astronomical Society of the Pacific, 2014, vol. 126, p. 459

Meyers R. A., Encyclopedia of physical science and technology. Academic, 2002

Mikulášek Z., Krtička J., Henry G. W., Zverko J., Žižňovskỳ J., Bohlender D., Romanyuk I. I., Janík J., Božić H., Korčáková D., et al., The extremely rapid rotational braking of the magnetic helium-strong star HD 37776, Astronomy & Astrophysics, 2008, vol. 485, p. 585

Neiner C., Landstreet J., Alecian E., Owocki S., Kochukhov O., Bohlender D., HD 96446: a puzzle for current models of magnetospheres?, Astronomy & Astrophysics, 2012, vol. 546, p. A44

Oksala M. E., Wade G. A., Marcolino W. L., Grunhut J., Bohlender D., Manset N., Townsend R. H., Discovery of a strong magnetic field in the rapidly rotating B2 Vn star HR 7355, Monthly Notices of the Royal Astronomical Society: Letters, 2010, vol. 405, p. L51

Pedersen H., Thomsen B., Spectrum and photometric variability of He-weak and He-strong stars, Astronomy and Astrophysics Supplement Series, 1977, vol. 30, p. 11

Petit V., Owocki S., Wade G., Cohen D. H., Sundqvist J., Gagné M., Apellániz J. M., Oksala M., Bohlender D., Rivinius T., et al., A magnetic confinement versus rotation classification of massive-star magnetospheres, Monthly Notices of the Royal Astronomical Society, 2013, vol. 429, p. 398

Prusti T., De Bruijne J., Brown A. G., Vallenari A., Babusiaux C., Bailer-Jones C., Bastian U., Biermann M., Evans D. W., Eyer L., et al., The gaia mission, Astronomy & astrophysics, 2016, vol. 595, p. A1

Rivinius T., Townsend R., Kochukhov O., Štefl S., Baade D., Barrera L., Szeifert T., Basic parameters and properties of the rapidly rotating magnetic helium-strong B star HR 7355, Monthly Notices of the Royal Astronomical Society, 2013, vol. 429, p. 177

Rubinho M. S., Damineli A., Carciofi A., Moser D., HD151018: strong magnetic field in a giant O-type star?, Proceedings of the International Astronomical Union, 2016, vol. 12, p. 442

Serkowski K., , 1974 in , Vol. 12, Methods in Experimental Physics. Elsevier pp 361–414

Serkowski K., Mathewson D., Ford V., Wavelength dependence of interstellar polarization and ratio of total to selective extinction, The Astrophysical Journal, 1975, vol. 196, p. 261

Shatsky N., Tokovinin A., The mass ratio distribution of B-type visual binaries in the Sco OB2 association, Astronomy & Astrophysics, 2002, vol. 382, p. 92

Shore S. N., Bohlender D., Bolton C., North P., Hill G., Magnetically controlled circumstellar plasma in the helium-weak stars, Astronomy & Astrophysics, 2004, vol. 421, p. 203

Shultz M. E., Wade G., Rivinius T., Neiner C., Alecian E., Bohlender D., Monin D., Sikora J., MiMeS Collaborations B., The magnetic early B-type stars I: magnetometry and rotation, Monthly Notices of the Royal Astronomical Society, 2018, vol. 475, p. 5144

Sikora J., Wade G., Bohlender D., Shultz M., Adelman S., Alecian E., Hanes D., Monin D., Neiner C., MiMeS Collaborations B., HD 35502: a hierarchical triple system with a magnetic B5IVpe primary, Monthly Notices of the Royal Astronomical Society, 2016, vol. 460, p. 1811

Smartt S. J., Progenitors of core-collapse supernovae, Annual Review of Astronomy and Astrophysics, 2009, vol. 47, p. 63

Stibbs D., A study of the spectrum and magnetic variable star HD 125248, Monthly Notices of the Royal Astronomical Society, 1950, vol. 110, p. 395

Stokes G. G., On the composition and resolution of streams of polarized light from different sources, Transactions of the Cambridge Philosophical Society, 1851, vol. 9, p. 399

Thomson J. J., Conduction of electricity through gases. University press, 1906

Tody D., IRAF in the Nineties. In Astronomical Data Analysis Software and Systems II , vol. 52, 1993, p. 173

Townsend R., Oksala M., Cohen D. H., Owocki S., et al., Discovery of rotational braking in the magnetic helium-strong star sigma Orionis E, The Astrophysical Journal Letters, 2010, vol. 714, p. L318

Townsend R., Owocki S., A rigidly rotating magnetosphere model for circumstellar emission from magnetic OB stars, Monthly Notices of the Royal Astronomical Society, 2005, vol. 357, p. 251

Townsend R., Owocki S., Groote D., The rigidly rotating magnetosphere of σ Orionis E, The Astrophysical Journal, 2005, vol. 630, p. L81

Ud-Doula A., Owocki S. P., et al., Dynamical simulations of magnetically channeled line-driven stellar winds. I. Isothermal, nonrotating, radially driven flow, The Astrophysical Journal, 2002, vol. 576, p. 413

Ud-Doula A., Owocki S. P., Townsend R. H., Dynamical simulations of magnetically channelled line-driven stellar winds–II. The effects of field-aligned rotation, Monthly Notices of the Royal Astronomical Society, 2008, vol. 385, p. 97

Wade G., Fullerton A., Donati J.-F., Landstreet J., Petit P., Strasser S., The magnetic field and confined wind of the O star Orionis C, Astronomy & Astrophysics, 2006, vol. 451, p. 195

Wade G., Grunhut J., Alecian E., Neiner C., Aurière M., Bohlender D., David-Uraz A., Folsom C., Henrichs H., Kochukhov O., et al., The magnetic characteristics of Galactic OB stars from the MiMeS survey of magnetism in massive stars, Proceedings of the International Astronomical Union, 2013, vol. 9, p. 265

Wade G., Grunhut J., Gräfener G., Howarth I., Martins F., Petit V., Vink J., Bagnulo S., Folsom C., Nazé Y., et al., The spectral variability and magnetic field characteristics of the Of? p star HD 148937, Monthly Notices of the Royal Astronomical Society, 2012, vol. 419, p. 2459

Wade G., Howarth I., Townsend R., Grunhut J., Shultz M., Bouret J.-C., Fullerton A., Marcolino W., Martins F., Nazé Y., et al., Confirmation of the magnetic oblique rotator model for the Of? p star HD 191612, Monthly Notices of the Royal Astronomical Society, 2011, vol. 416, p. 3160

Wade G., Neiner C., Alecian E., Grunhut J., Petit V., Batz B. d., Bohlender D., Cohen D. H., Henrichs H., Kochukhov O., et al., The MiMeS survey of magnetism in massive stars: introduction and overview, Monthly Notices of the Royal Astronomical Society, 2016, vol. 456, p. 2

Walborn N. R., A New Phenomenon in the Spectrum of Sigma Orionis E, The Astrophysical Journal, 1974, vol. 191, p. L95

Walder R., Folini D., Meynet G., Magnetic fields in massive stars, their winds, and their nebulae, Space science reviews, 2012, vol. 166, p. 145

Wardle J., Kronberg P., The linear polarization of quasi-stellar radio sources at 3.71 and 11.1 centimeters, The Astrophysical Journal, 1974, vol. 194, p. 249

Zahn J.-P., Brun A., Mathis S., On magnetic instabilities and dynamo action in stellar radiation zones, Astronomy & Astrophysics, 2007, vol. 474, p. 145

Appendix

Appendix A

Phase Coverage

In this appendix we present the data points and current state of the 13 magnetic stars with a incomplete phase coverage (see Table 4.1). As the survey unfolds and we complete the phase coverage, their data will be applied to the D+D model. Black and blue are the Stokes parameters Q and U respectively. Red is the observed polarization and the angle of polarization is green.

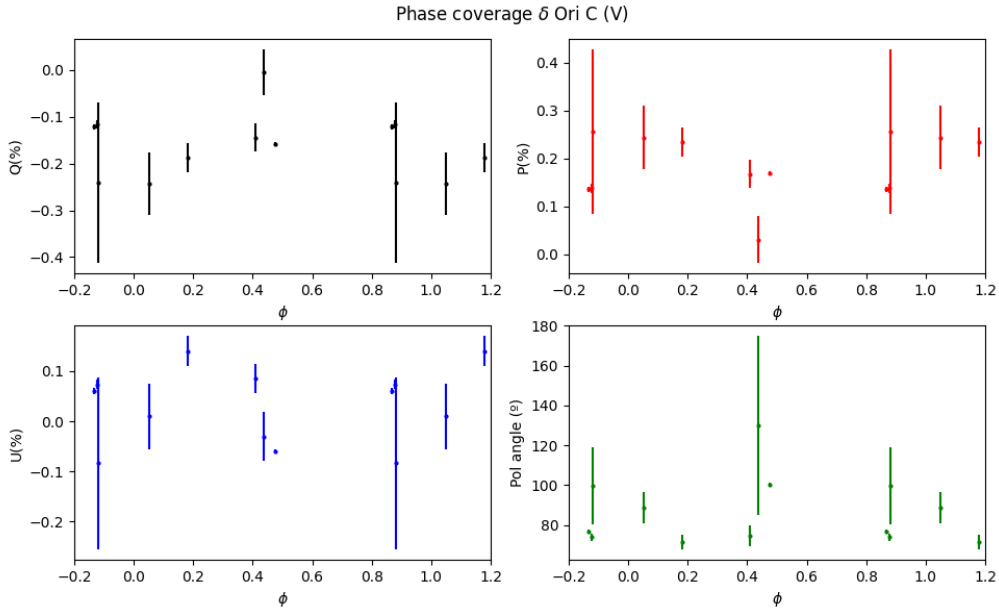

Figure A.1: Phase coverage of δ Ori C

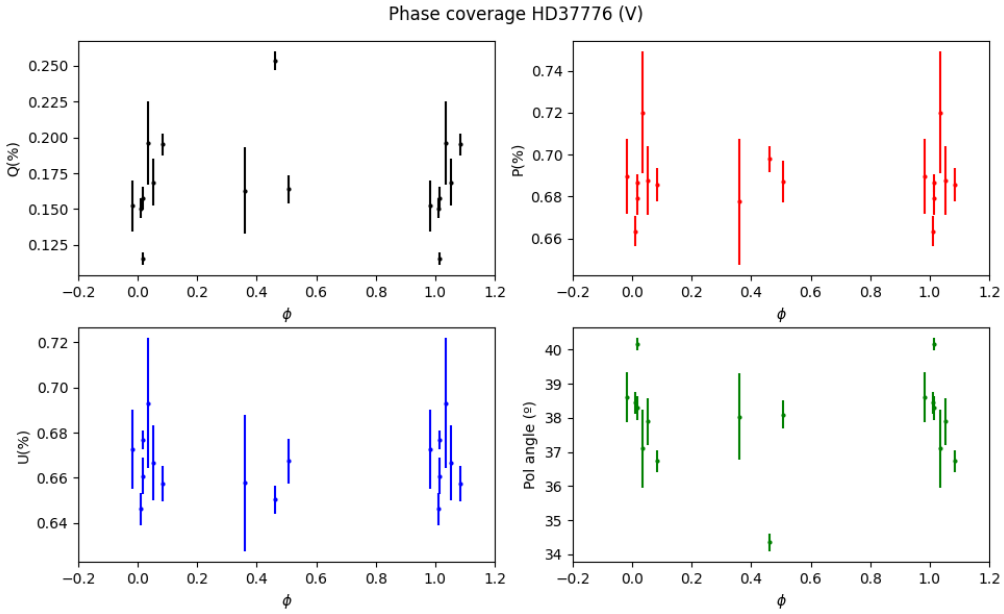

Figure A.2: Phase coverage of HD 37776.

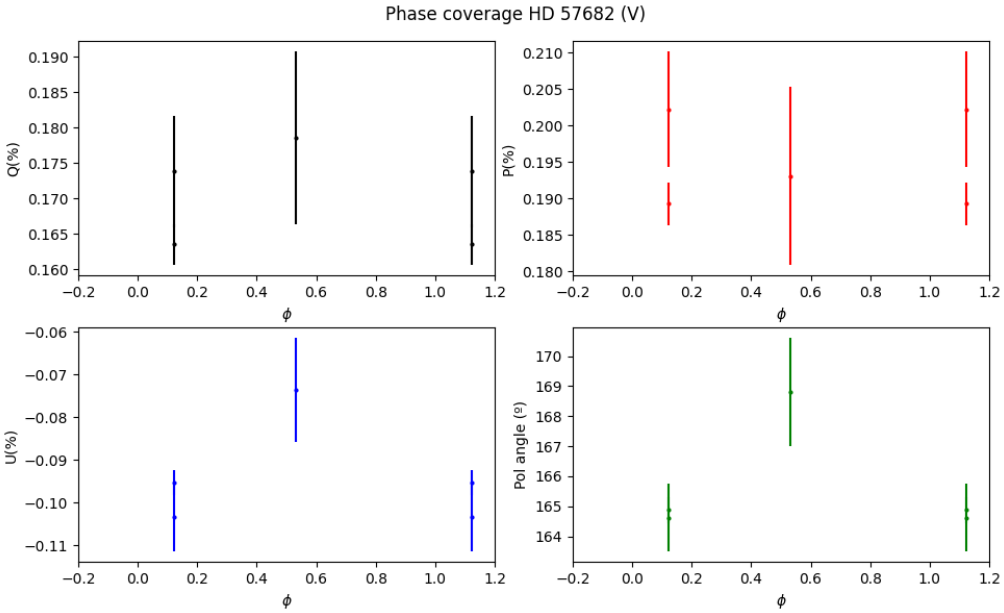

Figure A.3: Phase coverage of HD 57682.

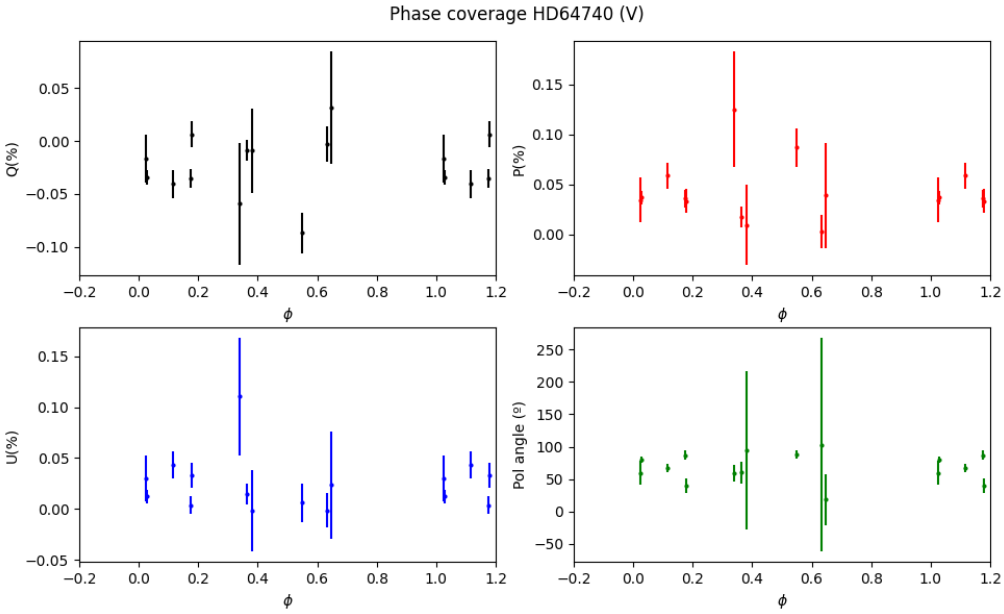

Figure A.4: Phase coverage of HD 64740.

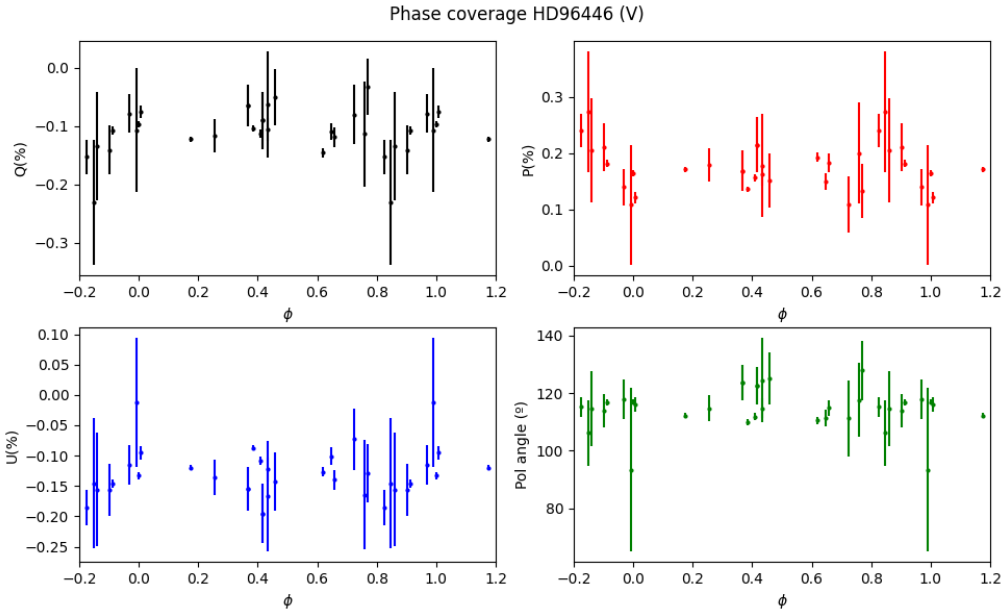

Figure A.5: Phase coverage of HD 96446.

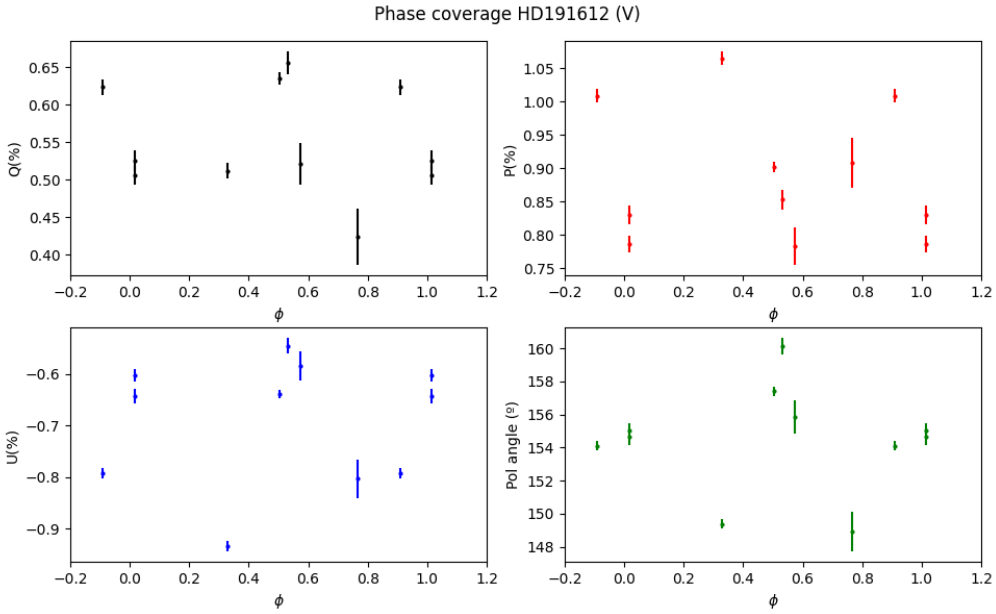

Figure A.6: Phase coverage of HD 191612.

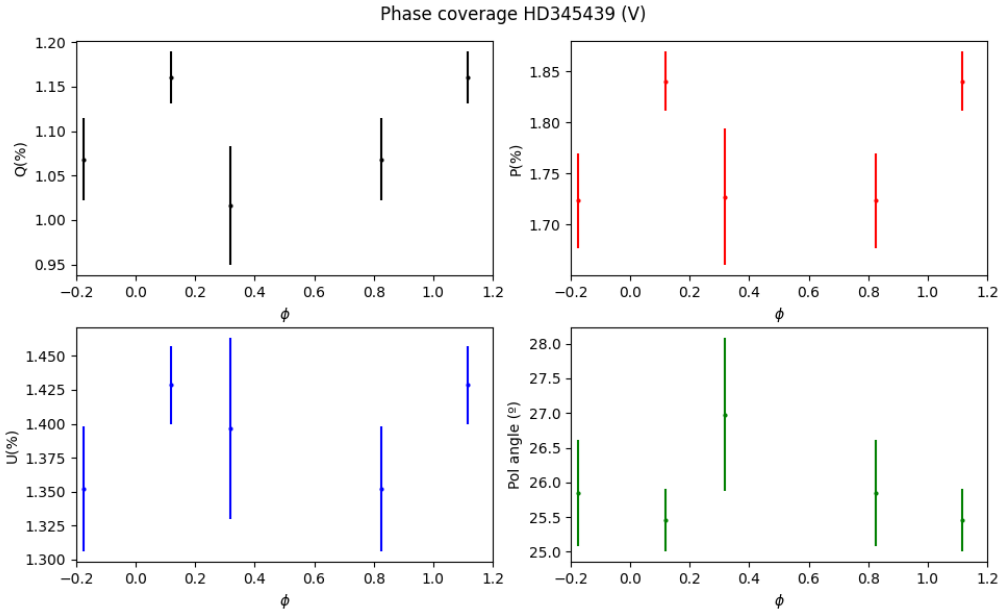

Figure A.7: Phase coverage of HD 345439.

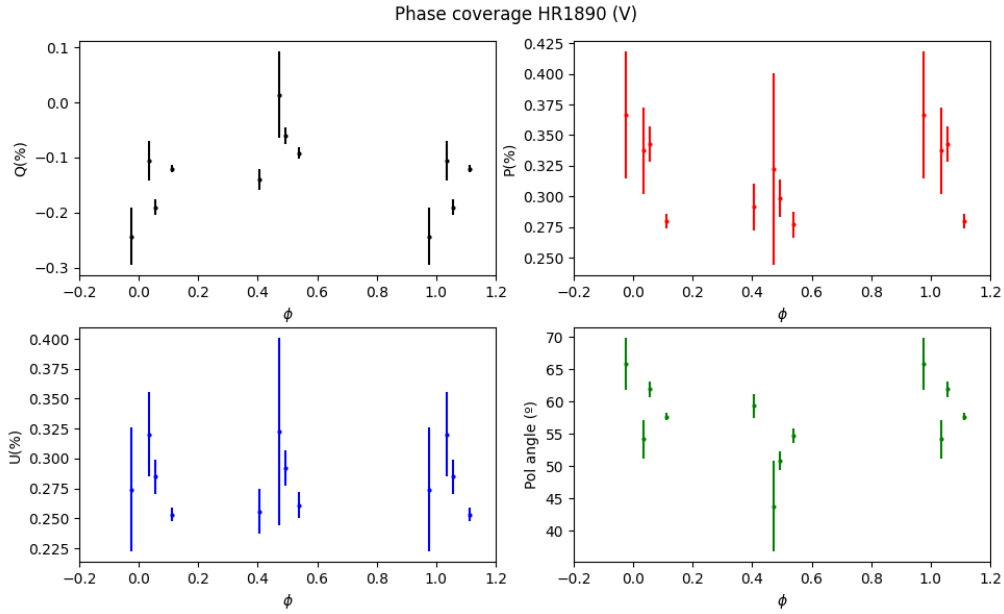

Figure A.8: Phase coverage of HD 37017.

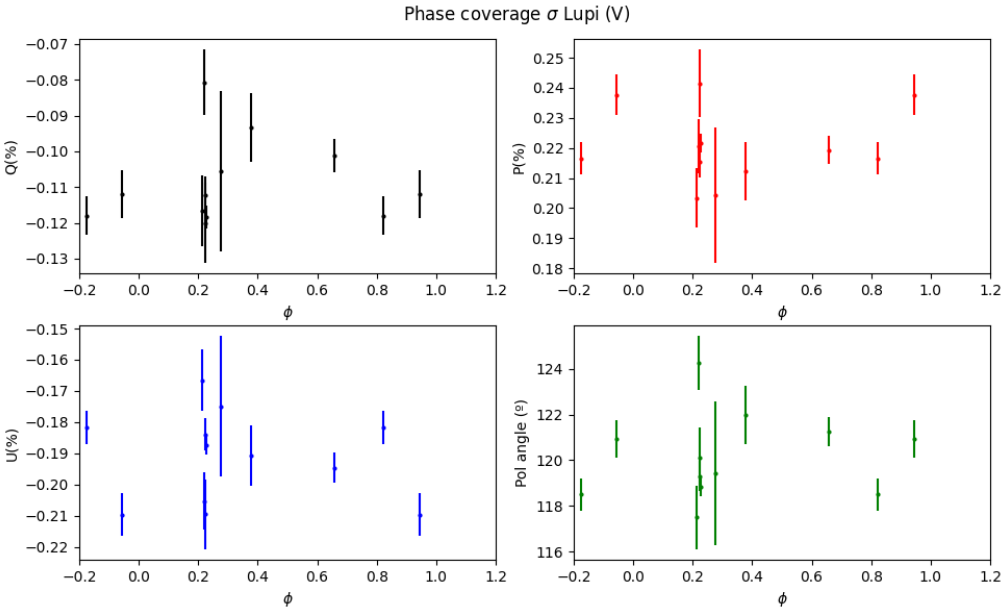

Figure A.9: Phase coverage of σ Lupi.

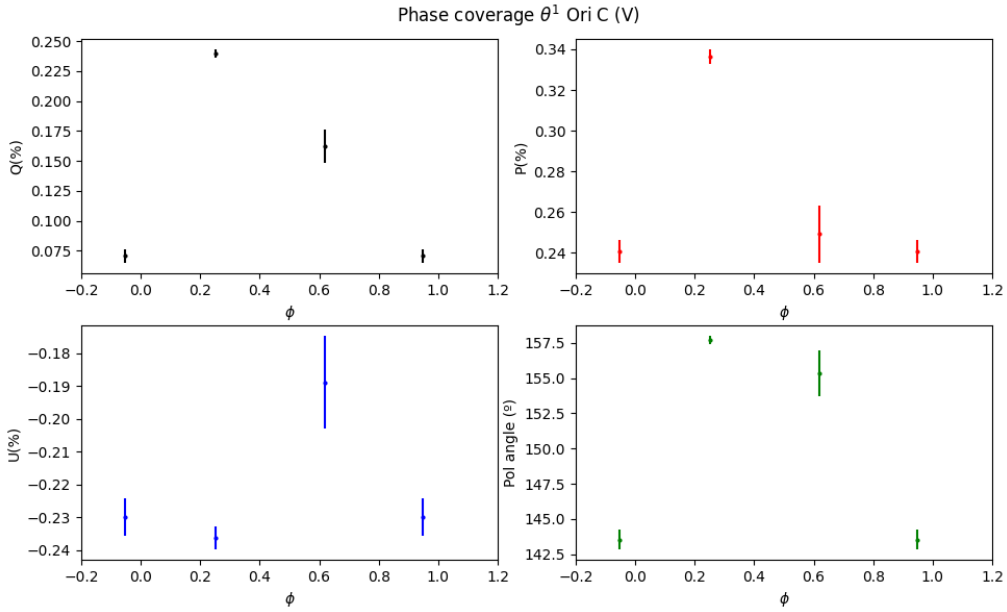

Figure A.10: Phase coverage of θ^1 Ori C.

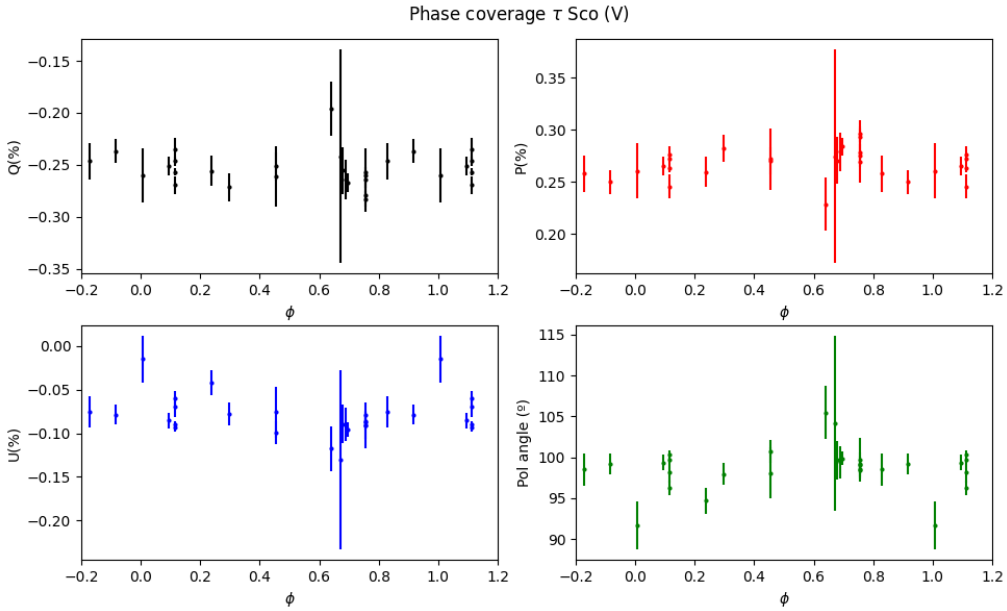

Figure A.11: Phase coverage of τ Sco.

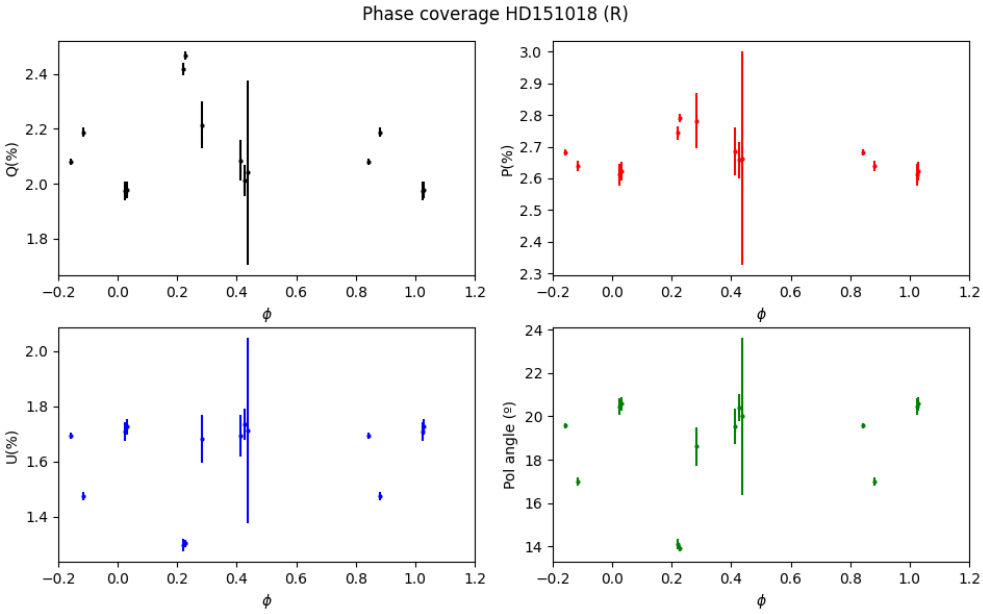

Figure A.12: Phase coverage of HD 151018.

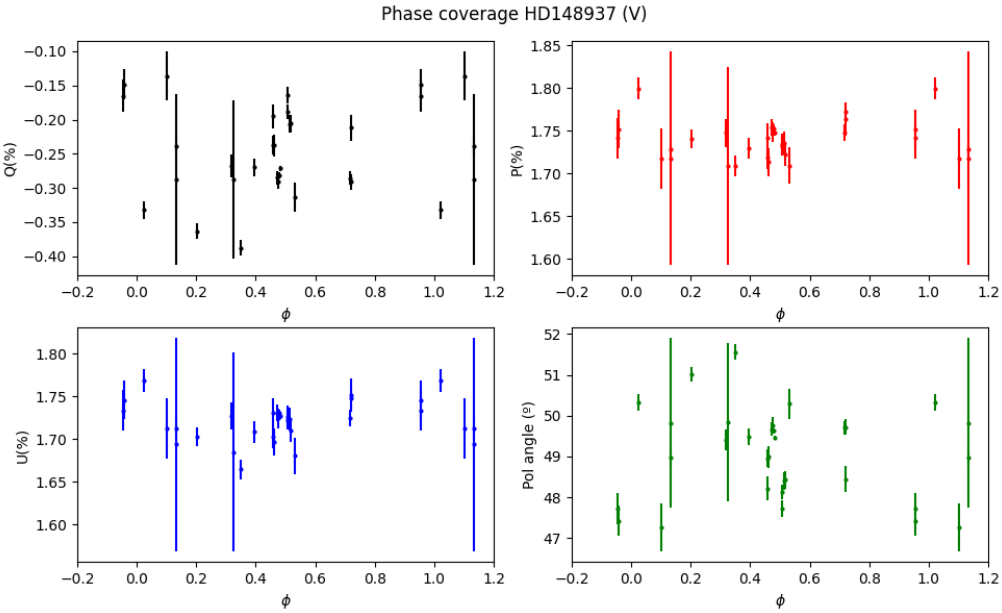

Figure A.13: Phase coverage of HD 148937.

Appendix B

Field Stars

In this chapter we present the polarization maps of the fields stars used to calculate the interstellar polarization of HD 35502, HR 7355, HR 5907. By selecting stars with no intrinsic polarization and physically close to the studied magnetic stars, the measured value is considered to originate in the interstellar medium. This method provides a reasonable estimate of the interstellar polarization of the magnetic star and was used as priors in our code.

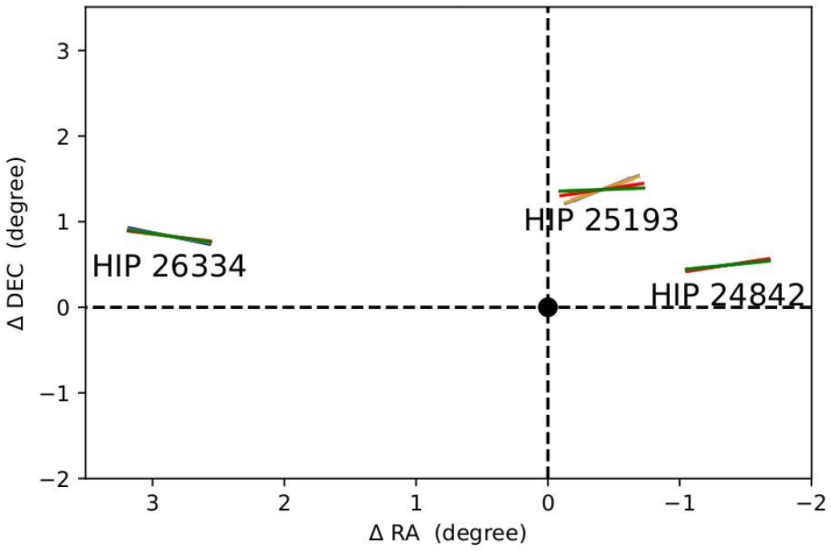

Figure B.1: Polarization map for the field of HD 35502, represented as a black dot at the origin. The direction of each vector represents the polarization measured for each filter observed.

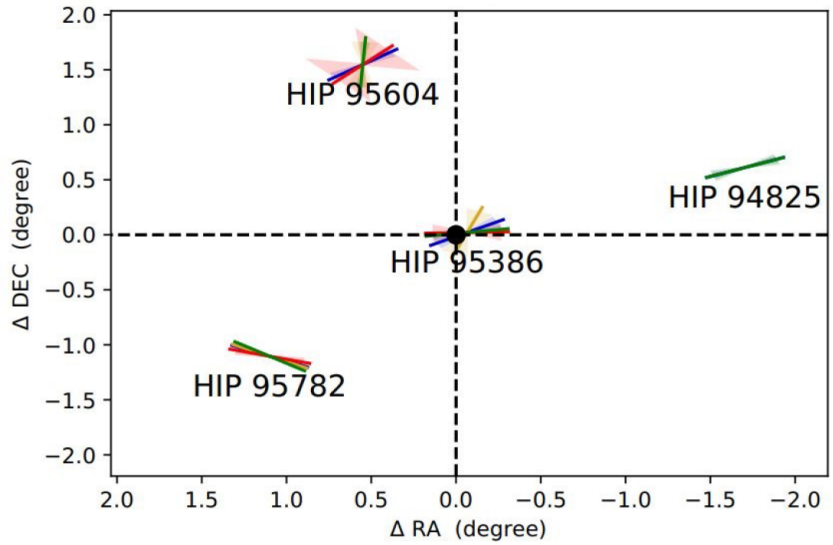

Figure B.2: Same as Fig. B.1 for HR 7355.

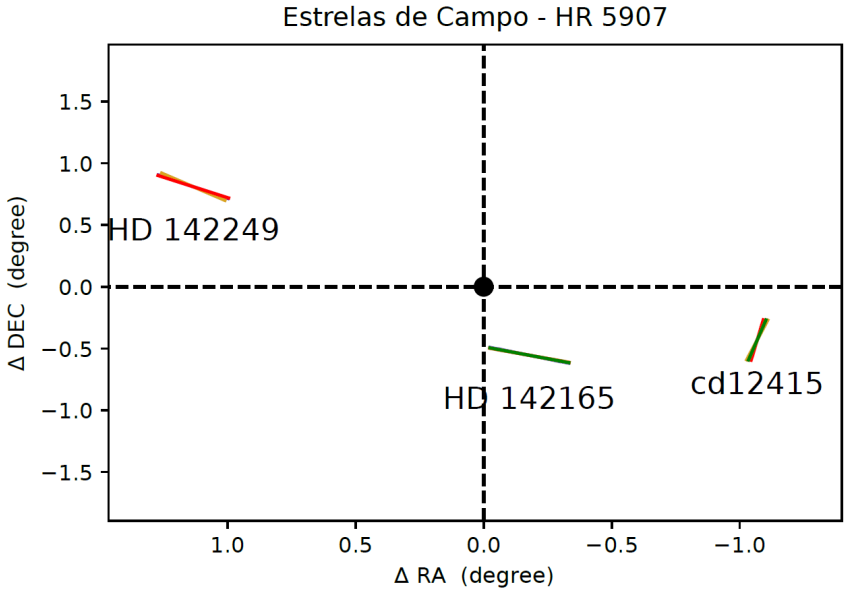

Figure B.3: Same as Fig. B.1 for HR 5907. The results are preliminar, and the star CD 12415 was not considered in the calculations.